GRB 130427A: a Nearby Ordinary Monster

A. Maselli[1*], A. Melandri[2], L. Nava[2,3], C.G. Mundell[4], N. Kawai[5,6],
S. Campana[2], S. Covino[2], J.R. Cummings[7], G. Cusumano[1], P.A. Evans[8],
G. Ghirlanda[2], G. Ghisellini[2], C. Guidorzi[9], S. Kobayashi[4], P. Kuin[10],
V. La Parola[1], V. Mangano[1,11], S. Oates[10], T. Sakamoto[12], M. Serino[6],
F. Virgili[4], B.-B. Zhang[11], S. Barthelmy[13], A. Beardmore[8], M.G. Bernardini[2],
D. Bersier[4], D. Burrows[11], G. Calderone[2,14], M. Capalbi[1], J.Chiang[15],
P. D'Avanzo[2], V. D'Elia[16,17], M. De Pasquale[10], D. Fugazza[2], N. Gehrels[13],
A. Gomboc[18,19], R. Harrison[4], H. Hanayama[20], J. Japelj[18], J. Kennea[11],
D. Kopac[18], C. Kouveliotou[21], D. Kuroda[22], A. Levan[23], D. Malesani[24],
F. Marshall[13], J. Nousek[11], P. O'Brien[8], J.P. Osborne[8], C. Pagani[8],
K.L. Page[8], M. Page[10], M. Perri[16,17], T. Pritchard[11], P. Romano[1], Y. Saito[5],
B. Sbarufatti[2,11], R. Salvaterra[25], I. Steele[4], N. Tanvir[8], G. Vianello[15],
B. Wiegand[13], K. Wiersema[8], Y. Yatsu[5], T. Yoshii[5], & G. Tagliaferri[2]

[*]To whom correspondence should be addressed; E-mail: maselli@ifc.inaf.it

[1]INAF-IASF Palermo, Via Ugo La Malfa 153 I-90146 Palermo, Italy; [2]INAF-Osservatorio Astronomico di Brera,
via E. Bianchi 46, I-23807 Merate, Italy; [3]APC, Université Paris Diderot, CNRS/IN2P3, CEA/Irfu, Observatoire
de Paris, Sorbonne Paris Cité, France; [4]Astrophysics Research Institute, Liverpool John Moores University, Liverpool Science Park, 146 Brownlow Hill, Liverpool L3 5RF, UK; [5]Department of Physics, Tokyo Institute of
Technology, 2-12-1 Ookayama, Meguro-ku, Tokyo 152-8551, Japan; [6]Coordinated Space Observation and Experiment Research Group, RIKEN, 2-1 Hirosawa, Wako, Saitama 351-0198, Japan; [7]UMBC/CRESST/NASA
Goddard Space Flight Center, Code 661, Greenbelt, MD 20771, USA; [8]Department of Physics and Astronomy,
University of Leicester, Leicester, LE1 7RH, UK; [9]Department of Physics, University of Ferrara, via Saragat 1,
I-44122, Ferrara, Italy; [10]Mullard Space Science Laboratory, University College London, Holmbury St. Mary,

Dorking, Surrey RH5 6NT, UK; [11]Department of Astronomy & Astrophysics, The Pennsylvania State University, 525 Davey Lab, University Park, PA 16802, USA; [12]Department of Physics and Mathematics, Aoyama Gakuin University, 5-10-1 Fuchinobe, Chuo-ku, Sagamihara, Kanagawa 252-5258, Japan; [13]NASA Goddard Space Flight Center, Greenbelt, MD 20771, USA; [14]Dipartimento di Fisica "G. Occhialini", Università di Milano-Bicocca, Piazza della Scienza 3, I-20126 Milano, Italy; [15]W. W. Hansen Experimental Physics Laboratory, Kavli Institute for Particle Astrophysics and Cosmology, Department of Physics, and SLAC National Accelerator Laboratory, Stanford University, Stanford, CA 94305, USA; [16]INAF/Rome Astronomical Observatory, via Frascati 33, 00040 Monteporzio Catone (Roma), Italy; [17]ASI Science Data Centre, Via Galileo Galilei, 00044 Frascati (Roma), Italy; [18]Faculty of Mathematics and Physics, University of Ljubljana, Jadranska 19 1000, Ljubljana, Slovenia; [19]Centre of Excellence Space-si, Aškerčeva cesta 12, 1000 Ljubljana, Slovenia; [20]Ishigakijima Astronomical Observatory, National Astronomical Observatory of Japan, 1024-1 Arakawa, Ishigaki, Okinawa 907-0024, Japan; [21]Space Science Office, VP62, NASA/Marshall Space Flight Center, Huntsville, AL 35812, USA; [22]Okayama Astrophysical Observatory, National Astronomical Observatory of Japan, 3037-5 Honjo, Kamogata, Asaguchi, Okayama 719-0232; [23]Department of Physics, University of Warwick, Coventry CV4 7AL, UK; [24]Dark Cosmology Centre, Niels Bohr Institute, University of Copenhagen, Juliane Maries Vej 30, 2100 Copenhagen, Denmark; [25]INAF-IASF Milano, via E. Bassini 15, I-20133 Milano, Italy

Long-duration Gamma-Ray Bursts (GRBs) are an extremely rare outcome of the collapse of massive stars, and are typically found in the distant Universe. Because of its intrinsic luminosity ($L \sim 3 \times 10^{53}$ erg s^{-1}) and its relative proximity ($z = 0.34$), GRB 130427A was a unique event that reached the highest fluence observed in the γ-ray band. Here we present a comprehensive multi-wavelength view of GRB 130427A with *Swift*, the 2-m Liverpool and Faulkes telescopes and by other ground-based facilities, highlighting the evolution of the burst emission from the prompt to the afterglow phase. The properties of GRB 130427A are similar to those of the most luminous, high-redshift GRBs, suggesting that a common central engine is responsible for producing GRBs in both the contemporary and the early Universe and over the full range of GRB isotropic energies.

GRB 130427A was the brightest burst detected by *Swift* (*1*) as well as by several γ–ray detectors onboard other space missions. It was also the brightest and longest burst detected above 100 MeV, with the most energetic photon detected at 95 GeV (*2*). It was detected by *Fermi*-GBM (*3*) at $T_{0,\mathrm{GBM}} = 07{:}47{:}06.42$ UT on April 27 2013. Hereafter this time will be our reference time T_0. The Burst Alert Telescope (BAT, (*4*)) onboard *Swift* triggered on GRB 130427A at t = 51.1 s, when *Swift* completed a pre-planned slew. The *Swift* slew to the source started at t = 148 s and ended at t = 192 s. The *Swift* UltraViolet Optical Telescope (UVOT, (*5*)) began observations at t = 181 s while observations by the *Swift* X–ray Telescope (XRT, (*6*)) started at t = 195 s (see (*7*) for more details). The structure of the γ-ray light curve revealed by the *Swift*-BAT in the 15–350 keV band (Fig. 1) can be divided in three main episodes: an initial peak, beginning at t = 0.1 s and peaking at t = 0.5 s; a second large peak showing a complex

structure with a duration of ~ 20 s and a third, much weaker episode, starting at t ~ 120 s showing a fast rise/exponential decay behavior. The overall duration of the prompt emission was T_{90} $(15-150 \text{ keV}) = 276 \pm 5$ s (i.e. the time containing 90% of the fluence) calculated over the first 1830 s of BAT observation from $T_{0,\text{GBM}}$. During the early phases of the γ-ray emission strong spectral variability is observed (Fig. 1). A marked spectral hardening is observed during the prompt main event. With a total fluence $F = (4.985 \pm 0.002) \times 10^{-4}$ erg cm^{-2} in the 15– 150 keV band, GRB 130427A reached the highest fluence observed for a GRB by *Swift*. The 0.02–10 MeV fluence measured by Konus-Wind (*8*) for the main emission episode $(0 - 18.7$ s$)$ is $(2.68 \pm 0.01) \times 10^{-3}$ erg cm^{-2}, with a spectrum peaking at $E_{\text{peak}} = 1028 \pm 8$ keV, while the fluence of the emission episode at $(120 - 250$ s$)$ is $\sim 9 \times 10^{-5}$ erg cm^{-2}, with a spectrum peaking at ~ 240 keV (*9*).

This event was extremely bright also in the optical and it was immediately detected by various robotic telescopes: in particular, the Raptor robotic telescope detected a bright optical counterpart already at t = 0.5 s (*10*). Optical spectroscopy of the afterglow determined the redshift to be $z = 0.34$ (*11*); an UVOT UV grism spectrum (*7*) was also acquired. At this distance the rest frame 1 keV–10 MeV isotropic energy is $E_{\text{iso}} = 8.1 \times 10^{53}$ erg and the peak luminosity is $L_{\text{iso}} = 2.7 \times 10^{53}$ erg s^{-1}. According to the luminosity function of Salvaterra et al. (*12*) we expect one event like GRB 130427A every > 60 years. In the nearby Universe (i.e. $z \lesssim 0.4$, corresponding to an age of ~ 10 Gyr) only a handful of long GRBs have been detected. These GRBs are usually characterized by a low overall isotropic energy ($E_{\text{iso}} \leq 10^{52}$ erg) and are associated with supernovae (SNe) Ib/c, characterized by broad spectral lines indicating high expansion velocities, called hypernovae (*13*). GRB 130427A is instead a powerful GRB such as the ones typically detected at much higher redshifts ($z > 1$, with a mean $z \sim 2$ corresponding to an age of ~ 3 Gyr). The detection of a nearby and extremely powerful GRB gives us the opportunity to test, on the one hand, if this GRB has the same properties of the cosmological

GRBs and, on the other hand, if also such bright GRBs are associated with SNe. Up to now, SNe have been associated only to under (or mildly) energetic GRBs in the local Universe. Since a supernova associated with this burst, SN 2013cq, has been detected (*14*), we are now sure that SNe are also associated with very powerful GRBs, not only to low power bursts (see Fig. S6; see also Fig. 1 of (*14*)). Naive energetic arguments might suggest that in powerful GRBs there is not enough power left for a strong SN: GRB 130427A definitively proves that this is not the case.

The overall behavior of the X–ray afterglow light curve has been characterized with the main contribution of the XRT onboard *Swift* and two additional relevant detections from the MAXI experiment (*15*) in the gap between the first and the second *Swift*-XRT observations (Fig. 2). The early light curve, starting from t = 260 s, is characterized by an initially steep decay with a slope $\alpha_{0,x}$ = 3.32 $\pm$ 0.17 consistent with high-latitude emission (*16, 17*), a break at $t_{1,x}$ = 424 $\pm$ 8 s followed by a flatter decay with index $\alpha_{1,x}$ = 1.28 $\pm$ 0.01. A further break at $t_{2,x}$ = 48 $\pm$ 22 ks is statistically needed (3.8σ) to account for a further steepening to $\alpha_{2,x}$ = 1.35 $\pm$ 0.02 (all errors are derived for $\Delta\chi^2 = 2.7$).

Figure 2 also shows the light curves in the optical and UV derived from the UVOT as well as from ground-based telescopes (Liverpool telescope, Faulkes Telescope North, and MITSuME Telescopes). All optical light curves are well fitted by a broken power law with $\alpha_1 = 0.96 \pm 0.01$, $t_{break} = 37.4 \, ^{+4.7}_{-4.0}$ ks and $\alpha_2 = 1.36 \, ^{+0.01}_{-0.02}$. Fitting the X–ray light curve together with the optical ones, we find the same parameters from 26.6 ks onward, but to fit the early part of the X–ray light curve we need another power–law segment with a slope of $1.29 \, ^{+0.02}_{-0.01}$ and a break at $26.6^{+4.5}_{-6.6}$ ks (Fig. 2). Therefore, from 26.6 ks onward a common description of all the optical, UV and X–ray behavior is possible, while at earlier times an extra X–ray component is required.

We interpret the early X–ray light curve (up to 26.6 ks) as the superposition of a standard afterglow (i.e. forward shock emission) and either the prolonged activity of the central engine

or/and the contribution from the reverse shock emission (e.g. (*18–20*)). After 26.6 ks the optical and X–ray light curves share the same behavior and decay slopes (Fig. 2), including a break at $t_{\mathrm{break}} \sim 37$ ks. This achromatic break is suggestive of a jet break, although the post-break decay ($\alpha_2 = 1.36$) is shallower than predicted in the simplest theory (an increase in decay slope > 1 would be expected; see (*21*)). This could be due to additional components contributing to the flux, to a time dependence of the microphysical parameters governing the fraction of shock energy going to electrons (ϵ_{e}) and magnetic field (ϵ_{B}), or to the fact that we observe a canonical jet not exactly on axis, but still within the jet opening angle (*22, 23*).

Because the optical and the X–ray emission belong to the same spectral power–law segment it is possible to constrain the characteristic frequencies of the afterglow spectra, in turn constraining the microphysical parameters of the relativistic shock. Additional information comes from the high-energy γ-ray emission (*2*). The γ–ray flux above 100 MeV peaks at ~ 20 s. If this emission is due to afterglow radiation, the peak time implies a bulk Lorentz factor $\Gamma_0 \sim 500$ (*2, 7*). Furthermore, the presence of the GeV peak suggests a homogeneous circumburst density profile (*24*). Guided by these constraints in our choice of parameters, we used the BOXFIT code developed by van Eerten et al. (*25*) to model the afterglow. Rather than trying to perform a formal fit to the data we check if this burst, with an unprecedented data coverage and richness, can be interpreted in the framework of the standard model for the afterglow emission, or else if it forces us to abandon the standard framework. We give more weight to the optical and higher energy fluxes, since they carry most of the afterglow luminosity, orders of magnitude greater than the radio flux.

Neither reverse shock nor inverse Compton (IC) emission are included in the model, but this does not affect our conclusions which primarily concern the late time synchrotron afterglow (see (*7*) for further details). The synchrotron flux predicted by the model reproduces the optical emission and the X–ray light curve after ~ 10 ks reasonably well, while the early X–ray flux is

likely due to an additional component (Fig. 3). Our model underestimates the GeV emission but this, given the large $\epsilon_{\rm e}/\epsilon_{\rm B}$ ratio, can be due to synchrotron Self–Compton emission, as envisaged by (*2, 26, 27*). The model can also roughly reproduce the radio emission (further details in (*7*)).

Consistent with the light curve analysis, the synchrotron flux predicted by the model reproduces reasonably well the optical and X–ray parts of the spectral energy distribution (SED) of the afterglow (Fig. 4), but it underestimates the GeV emission. Although the model does not entirely reproduce the complexity shown by the data, it does capture the main features of the emission properties in the pure afterglow phase.

Overall, the properties of GRB 130427A are similar to those of the powerful GRBs typically seen at $z \sim 1-2$ (see (*7*) for a comparison). This is the most powerful GRB at $z < 0.9$. It obeys the spectral energy correlations such as the $E_{\rm peak} - E_{\rm iso}$ (*28*) correlation and the $E_{\rm peak} - L_{\rm peak}$ (*29*) correlation. Interpreting the break observed at ~ 37 ks as a jet break makes GRB 130427A consistent with the collimation corrected energy–peak energy correlation (*7,30*). GRB 130427A is also associated with a supernova, extending the GRB-SN connection also to such powerful and high–z bursts. GRB 130427A stands as a unique example indicating that a common engine is powering these huge explosions at all powers, and from the nearby to the very far, early Universe.

References and Notes

1. A. Maselli, *et al.*, *GRB Coordinates Network* **14448**, 1 (2013).

2. Fermi-LAT Team, *Science* (2013).

3. C. Meegan, *et al.*, *ApJ* **702**, 791 (2009).

4. S. D. Barthelmy, *et al.*, *Space Sci. Rev.* **120**, 143 (2005).

5. P. W. A. Roming, *et al.*, *Space Sci. Rev.* **120**, 95 (2005).

6. D. N. Burrows, *et al.*, *Space Sci. Rev.* **120**, 165 (2005).

7. Materials and methods are available as supplementary material on Science Online.

8. R. L. Aptekar, *et al.*, *Space Sci. Rev.* **71**, 265 (1995).

9. S. Golenetskii, *et al.*, *GRB Coordinates Network* **14487**, 1 (2013).

10. T. Vestrand, *et al.*, *Science* (2013).

11. A. J. Levan, S. B. Cenko, D. A. Perley, N. R. Tanvir, *GRB Coordinates Network* **14455**, 1 (2013).

12. R. Salvaterra, *et al.*, *ApJ* **749**, 68 (2012).

13. S. E. Woosley, J. S. Bloom, *ARA&A* **44**, 507 (2006).

14. D. Xu, *et al.*, *ApJ* **776**, 98 (2013).

15. M. Matsuoka, *et al.*, *PASJ* **61**, 999 (2009).

16. G. Tagliaferri, *et al.*, *Nature* **436**, 985 (2005).

17. J. A. Nousek, *et al.*, *ApJ* **642**, 389 (2006).

18. P. Mészáros, *Reports on Progress in Physics* **69**, 2259 (2006).

19. G. Ghisellini, M. Nardini, G. Ghirlanda, A. Celotti, *MNRAS* **393**, 253 (2009).

20. A. Panaitescu, W. T. Vestrand, *MNRAS* **414**, 3537 (2011).

21. R. Sari, T. Piran, J. P. Halpern, *ApJL* **519**, L17 (1999).

22. H. van Eerten, W. Zhang, A. MacFadyen, *ApJ* **722**, 235 (2010).

23. H. J. van Eerten, A. I. MacFadyen, *ApJ* **751**, 155 (2012).

24. L. Nava, L. Sironi, G. Ghisellini, A. Celotti, G. Ghirlanda, *MNRAS* **433**, 2107 (2013).

25. H. van Eerten, A. van der Horst, A. MacFadyen, *ApJ* **749**, 44 (2012).

26. R.-Y. Liu, X.-Y. Wang, X.-F. Wu, *ApJL* **773**, L20 (2013).

27. P.-H. T. Tam, Q.-W. Tang, S.-J. Hou, R.-Y. Liu, X.-Y. Wang, *ApJL* **771**, L13 (2013).

28. L. Amati, *et al.*, *A&A* **390**, 81 (2002).

29. D. Yonetoku, *et al.*, *ApJ* **609**, 935 (2004).

30. G. Ghirlanda, G. Ghisellini, D. Lazzati, *ApJ* **616**, 331 (2004).

31. T. Laskar, *et al.*, *ApJ* **776**, 119 (2013).

32. A. von Kienlin, *GRB Coordinates Network* **14473**, 1 (2013).

33. D. A. Perley, *GRB Coordinates Network* **14494**, 1 (2013).

34. P. Romano, *et al.*, *A&A* **456**, 917 (2006).

35. P. W. Roming, *et al.*, *Society of Photo-Optical Instrumentation Engineers (SPIE) Conference Series*, K. A. Flanagan, O. H. Siegmund, eds. (2000), vol. 4140 of *Society of Photo-Optical Instrumentation Engineers (SPIE) Conference Series*, pp. 76–86.

36. P. W. A. Roming, *et al.*, *Society of Photo-Optical Instrumentation Engineers (SPIE) Conference Series*, K. A. Flanagan, O. H. W. Siegmund, eds. (2004), vol. 5165 of *Society of Photo-Optical Instrumentation Engineers (SPIE) Conference Series*, pp. 262–276.

37. S. R. Oates, *et al.*, *MNRAS* **395**, 490 (2009).

38. M. J. Page, *et al.*, *MNRAS* **436**, 1684 (2013).

39. A. A. Breeveld, *et al.*, *MNRAS* **406**, 1687 (2010).

40. A. A. Breeveld, *et al.*, *American Institute of Physics Conference Series*, J. E. McEnery, J. L. Racusin, N. Gehrels, eds. (2011), vol. 1358 of *American Institute of Physics Conference Series*, pp. 373–376.

41. T. S. Poole, *et al.*, *MNRAS* **383**, 627 (2008).

42. T. Mihara, *et al.*, *PASJ* **63**, 623 (2011).

43. M. Sugizaki, *et al.*, *PASJ* **63**, 635 (2011).

44. N. R. Butler, D. Kocevski, *ApJ* **663**, 407 (2007).

45. P. A. Evans, *et al.*, *MNRAS* **397**, 1177 (2009).

46. R. Margutti, *et al.*, *MNRAS* **428**, 729 (2013).

47. C. Guidorzi, *et al.*, *PASP* **118**, 288 (2006).

48. Y. Saito, *et al.*, *Death of Massive Stars: Supernovae and Gamma-Ray Bursts* (2012), vol. 279 of *IAU Symposium*, pp. 387–388.

49. R. Sari, *ApJL* **489**, L37 (1997).

50. G. Ghirlanda, *et al.*, *MNRAS* **420**, 483 (2012).

51. S. Kobayashi, B. Zhang, *ApJ* **597**, 455 (2003).

52. D. A. Perley, *et al.*, *ApJ* **781**, 37 (2014).

53. A. Panaitescu, P. Kumar, *ApJL* **560**, L49 (2001).

54. P. Kumar, R. Barniol Duran, *MNRAS* **409**, 226 (2010).

55. G. Ghisellini, G. Ghirlanda, L. Nava, A. Celotti, *MNRAS* **403**, 926 (2010).

56. E. M. Rossi, D. Lazzati, J. D. Salmonson, G. Ghisellini, *MNRAS* **354**, 86 (2004).

57. T. Piran, E. Nakar, *ApJL* **718**, L63 (2010).

58. H. J. van Eerten, Z. Meliani, R. A. M. J. Wijers, R. Keppens, *MNRAS* **410**, 2016 (2011).

59. A. Panaitescu, *Nuovo Cimento B Serie* **121**, 1099 (2006).

60. L. Nava, *et al.*, *MNRAS* **421**, 1256 (2012).

61. D. J. Schlegel, D. P. Finkbeiner, M. Davis, *ApJ* **500**, 525 (1998).

62. M. Fukugita, *et al.*, *AJ* **111**, 1748 (1996).

Figure 1. Details of the *Swift* BAT light curve in the 15–350 keV band. Top panel: the BAT light curve with a binning time of 64 ms. Inset: the BAT light curve up to 300 s, plotted on a log intensity scale, showing a fast rise/exponential decay feature starting at t $\sim$ 120 s. Bottom panel: the photon index values of a power-law model fit to the BAT spectrum in the 15–150 keV energy range.
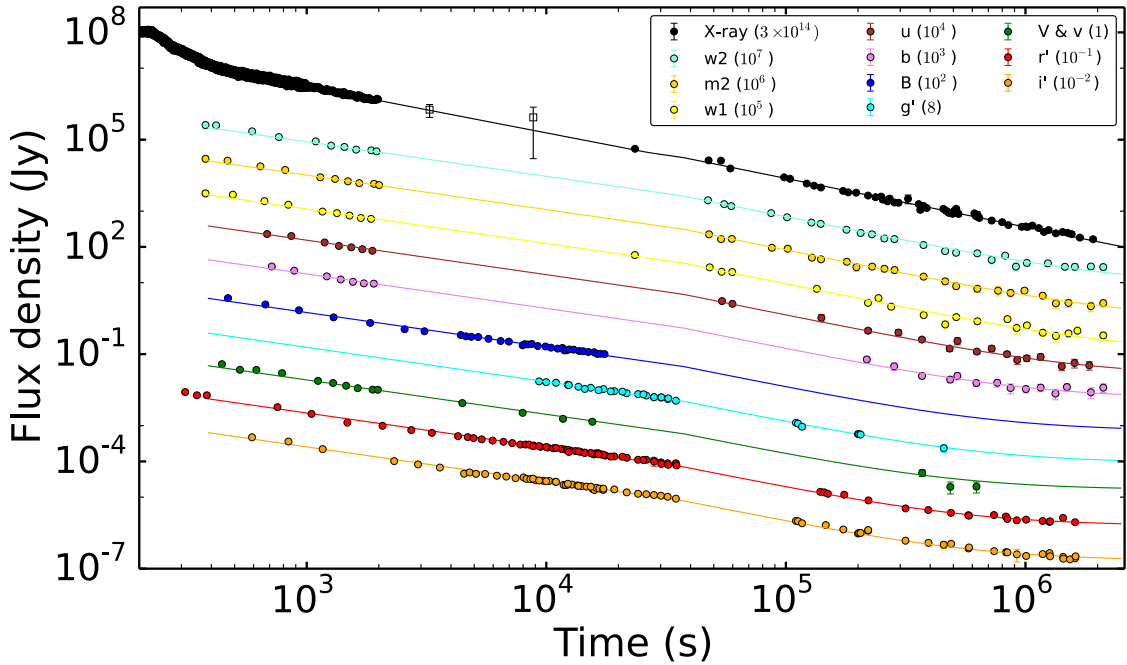
Figure 2: Light curves for GRB 130427A in different wavebands. *Swift* UV and visible filters ($w2$, $m2$, $w1$, u, b, v); B, V, r', and i' filters correspond to Faulkes Telescope North; r', and i' to the Liverpool Telescope; g', r', and i' to the MITSuME telescopes (see *7* for further details). The scaling factors for the flux density in different filters is shown in the inset; the scaling factor for the X–ray light curve (flux integrated in the 0.3–10 keV, see *7*) is also shown. The X–ray light curve also includes two MAXI data points at t = 3257 s and t = 8821 s (empty squares). The fit performed over all the light curves required 24 free parameters (curve normalizations, host galaxy optical flux in each band, three temporal slopes and two breaks). Because of short-term low-level variability superposed to the long-term behavior and possibly residual inhomogeneity of optical data taken from different telescopes, we added in quadrature a 9% systematic error in the optical and 5% in the X–rays. Final fit yielded χ^2 = 543.02 / 565 d.o.f. A contribution from the host galaxy has been taken into account in the optical bands by fitting a constant flux of $\sim$ 0.01 mJy for the reddest bands, corresponding to r_{HG} = 21.26 mag as tabulated in the SDSS catalogue. As a test of consistency, we performed the fit using a broken power law for the B, g', r' and i' filters individually. Uncertainties are larger, but we do find that the values of t_{break} as well as the decay indices before and after the break time are still consistent, within the errors, with the values obtained by the overall fit.
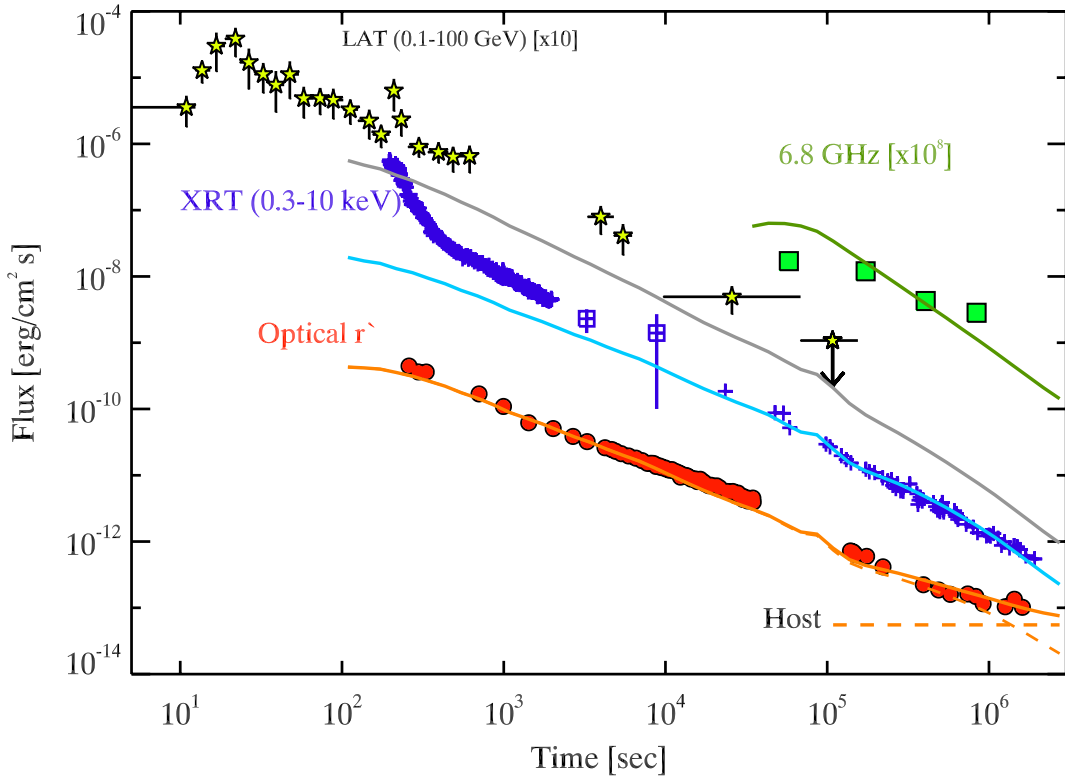
Figure 3. Radio (from *31*: all measurements are taken at 6.8 GHz but the later one, at 7.3 GHz), optical, X–ray (Figure 2) and LAT γ-ray (from *2*) light curves of GRB 130427A and corresponding model predictions adopting a description in terms of the van Eerten et al. model (*25*). To properly fit the radio data, only a fraction of the electrons must be accelerated after ∼ 70 ks (see Table S10 and discussion in *7*).

15
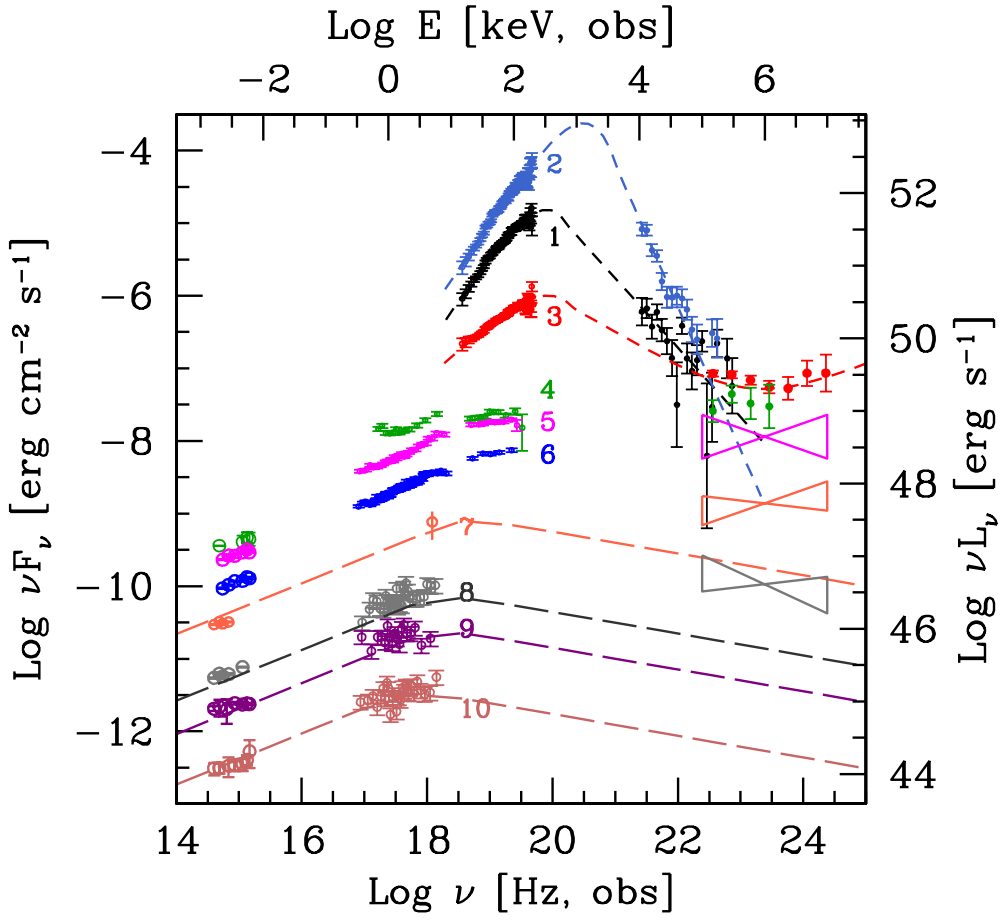
Figure 4. Spectral Energy Distributions (SEDs) of GRB 130427A taken at different times, from the optical to the GeV bands (LAT data from *2*). For SED 1 and SED 2 the model is a Band function, for SED 3 the model is a Band+power law. Short dashed lines: phenomenological fit to the BAT+LAT data. Long dashed lines: results of the van Eerten et al. model (*25*), with parameters discussed in (*7*). The different SEDs refer to the following time intervals: 1: [0–6.5 s]; 2: [7.5–8.5 s]; 3: [8.5–196 s]; 4: [352–403 s]; 5: [406–722 s]; 6: [722–1830 s]; 7: around 3 ks; 8: around 23 ks; 9: around 59 ks; 10: around 220 ks (host galaxy contribution has been subtracted in this case). Note that from the optical SED analysis the intrinsic extinction is negligible.

Supplementary Materials

www.sciencemag.org

Materials and Methods

Figures S1, S2, S3, S4, S5, S6, S7

Tables S1, S2, S3, S4, S5, S6, S7, S8, S9

References (32–62) [Note: The numbers refer to any additional references cited only within the

Supplementary Materials].

1   Observations and Data Analysis

1.1   *Swift* Discovery and Observations

1.1.1   BAT Observations

BAT triggered on GRB 130427A (*1*) at 2013-04-27 07:47:57.5 UTC (trigger # 554620) 51.1 seconds later than the *Fermi*-GBM trigger (*32*), after *Swift* completed a pre-planned slew. Hereafter, all times are referred to $T_{0,\mathrm{GBM}}$ so that $t = T - T_{0,\mathrm{GBM}}$. The BAT trigger was on the tail of the main peak, in a 64-second image trigger (see (*4*) for details on the BAT triggering system). The *Swift* slew to the source started at $t = 148$ s and ended at $t = 192$ s. The BAT position of the burst, initially calculated onboard and then refined in ground analysis, is $\mathrm{RA}_{J2000} = 11^h$ 32^m $36^s.1$, $\mathrm{Dec}_{J2000} = +27° \ 42' \ 20''.3$ with an uncertainty of $1'.0$ (radius, sys+stat, 90% containment); this is $49''.9$ from the radio afterglow position $\mathrm{RA}_{J2000} = 11^h \ 32^m \ 32^s.82$, $\mathrm{Dec}_{J2000} = +27° \ 41' \ 56''.06$ determined with a precision of $0''.4$ (*33*).

The BAT mask–weighted light curve in the 15–350 keV band is shown in Figure S1. A first pulse beginning at $t = 0.13$ s and peaking at $t = 0.5$ s is followed by another, smaller pulse at $t = 1.1$ s. Then the main episode of emission begins gradually at $t = 2.2$ s, with a sharp pulse at $t = 5.4$ s. A multi-peaked intense emission follows, lasting a total of about 5 seconds with a peak at $t \sim 8$ s. A few, less intense pulses follow on top of a decay from the main episode, with rise and decay on a time scale of a few seconds, the last peaking at about $t = 26$ s. There was some significant deadtime over the main peak of the event, that was corrected with a maximum correction factor of 1.72. At $t = 120$ s we have a fast rise with two overlapping pulses peaking at $t = 131$ s and $t = 141$ s, respectively, followed by an exponential decay. After $t = 270$ s there are no further prominent features. The decaying emission in the BAT energy range, well fit by a power-law model, was detectable until the end of the observation at $t = 2021$ s. BAT data corresponding to the last 1031 s were collected in survey mode.

18

1.1.2 XRT Observations

XRT data were accumulated in Windowed Timing (WT) and Photon Counting (PC) mode (*6*) depending on the brightness of the source. The pointed *Swift*-XRT observations of GRB 130427A started at t = 195 s in WT mode. Due to the loss of star tracker lock that occurred soon after the beginning of the observation, the attitude file needed for data reduction has been manually reconstructed using the UVOT data (see section 1.1.3) to provide time-dependent pointing corrections for the XRT data. For the subsequent observations the loss of star tracker lock occurred again for several further short time intervals: data affected by bad attitude reconstruction were adequately screened during the data reduction process. *Swift*-XRT observations that were used for this work include a total net exposure time of ∼1826 s in WT mode and ∼ 203 ks in PC mode up to the sequence 090, spread over a ∼ 4 Ms baseline. The XRT data set was first processed with the XRTDAS software package (v.2.8.0) developed at the ASI Science Data Center (ASDC) and distributed by HEASARC within the HEASoft package (v. 6.13). Event files were calibrated and cleaned with standard filtering criteria with the XRTPIPELINE task using the latest calibration files available in the *Swift* CALDB. Standard grade filtering was applied: 0–12 for PC data and 0–2 for WT data. The list of all XRT observations of GRB 130427A used for the present analysis is shown in Table S1.

The first XRT observation in WT mode partially overlaps the time interval during which BAT data are available, from its start until t = 990 s; the remaining part is given by 1031 s of data. The count rate of the first XRT observation was high enough to cause severe pile-up in the WT mode data. To account for this effect, the WT data were extracted in annular regions with a 60-pixel (1 pixel = 2.36″) external radius and a variable radius of the inner excluded region depending on the pile-up degree. The size of the exclusion region was determined following the procedure illustrated in (*34*). The values adopted for the inner radius are reported in Table S2.

Data from light curves and spectra relevant to observations in PC mode were extracted

using the task XRTGRBLC, that performs the appropriate corrections for vignetting and PSF losses. The task optimizes the extraction regions according to the count rate of the source in each orbit, excluding a central circular region in case of pile-up (sequences 001 to 013) whose radius is reported in Table S2. The background was extracted from an annular region with inner and outer radii 47 and 90 pixels, respectively. Ancillary response files were generated with the XRTMKARF task allowing us to correct for CCD defects. We used the latest CALDB response matrices (rmf): v013 (PC mode) and v014 (WT mode).

1.1.3 UVOT Observations

Swift Ultraviolet Optical Telescope (UVOT; (*5,35,36*)) began observing the burst at t = 181 s. During the automatic sequence, *Swift* was unable to obtain a positional lock using the onboard catalogue as there were too few guide stars in the field of view. The loss of star tracker lock caused the optical afterglow to wander across the image plane, so that with each consecutive exposure the afterglow position shifted increasingly in RA and Dec away from the reported position. For longer exposures this movement caused the point sources in the image to be trailed. Since these observations were taken in event mode (where the position and timing of each event are recorded down to a time resolution of 11 ms), we were able to aspect correct the observations to a finer time resolution than the duration of each exposure and recover the trailed sources as point sources. Because the observed and actual positions of the stars in the image were different by up to $\sim 300''$, the aspect correction was performed in a two-step process. First, a coarse aspect correction was determined manually for each exposure; then, a fine aspect correction was determined by extracting an image from the event list every 10 s and cross-correlating the stars in the image with those in the USNO-B1 catalogue. The differences in RA and Dec were then applied to each event falling within the particular 10 s interval (*37*).

During the first 2 ks of observations, the optical afterglow of GRB 130427A was so bright

that UVOT suffered from heavy coincidence losses and scattered light. The v-band 10 s settling point observed from t = 181 s, the majority of white data before T+2000 s, and the b and u band data observed before 650 s could not be recovered. However, using the read-out streaks (*38*) we were able to obtain photometry for the white band data between 506 and 1023 s and for the first b and u band exposures. Earlier and later saturated white data are beyond the recommended range for the read-out streak method. We were also able to obtain photometry from UVOT UV grism spectrum, which provides the earliest UVOT photometry for this GRB, by folding the spectrum through the filter response curves.

For the later follow-up observations, the star tracker obtained a positional lock on most images, but for the observations where it failed to lock the images are trailed or the point sources are blurred. Therefore, we manually inspected all exposures and excluded those that would produce unreliable photometry. For the aspect corrected event mode data, the photometry was obtained using the uvot tool UVOTEVTLC, while the image mode data were processed using the uvot tool UVOTMAGHIST. The photometry for the image and event mode observations were extracted using a circular aperture with a radius of $5''$ when the count rate was above 0.5 cts s^{-1}, and $3''$ aperture when the count rate had dropped below 0.5 cts s^{-1}; an appropriate background region was used. We applied coincidence loss corrections and standard photometric calibrations (*39-41*). The analysis pipeline used software HEASOFT 6.13 and UVOT calibration 20130118. The list of UVOT observations which were included in the analysis of GRB 130427A are shown in Table S3.

Since November 2008 the automated sequence that is triggered by a strong burst includes a 50-second UV grism exposure after the first white finder chart. A magnitude brighter than $v = 12$ mag is needed to get a GRB detection. GRB 130427A provided the second good early UV spectrum from the instrument.

The data reduction required special adaptations due to the loss of star tracker lock which

affected the normal processing. Using the data of detected photon positions in the white filter prior to the grism exposure in image mode, and assuming a steady motion, the spacecraft moved during the grism exposure by about $9.5''$(18 pixels) under an angle of $64°$ to the dispersion in the direction of longer wavelengths. Assuming a smooth motion, this translates into a shift of ≈ 54 Å in the dispersion direction.

The blurring effect of the motion on the grism image was determined by deconvolving a zeroth order of a fainter object in the grism image by a zeroth order from an image obtained during normal *Swift* operations, i.e., with attitude lock. The resulting kernel shows the exposure locations on the detector for that zeroth order and thus suggests that the exposure was mainly taken whilst the pointing rested in two locations about 7 pixels apart under an angle consistent with the analysis from the white filter event data. Using that kernel to deconvolve the grism image, a cleaner grism image was obtained where the effects of blurring are to a large extent removed. For the deconvolution the STARLINK LUCY program was used.

To determine the position of the spectrum on the detector, the last 5 seconds of the event data from the white filter finder were separately processed and aspect-corrected using the HEA-SOFT 6.13 tools. This image ended 5.5 s before the start of the grism exposure, so the position of the source on the detector in the white filter was known. Using the new grism calibration and related software (http://www.mssl.ucl.ac.uk/www_astro/uvot/) this was used to determine the location of the spectrum on the grism image and extract the spectrum with good knowledge of the wavelength scale.

The flux calibration used includes a correction for coincidence loss which is estimated to be in the range of 10-20% for this spectrum. There is partial overlap of second order emission, estimated to start affecting the flux above the observed wavelength of 3000 Å by 15%, slowly varying thereafter. The spectrum observed above 3000 Å can be used to some extent for the spectral lines present, for example, redshifted Mg II 2800 Å resonance line is present as one of

the strongest absorptions.

The *Swift* UVOT spectrum with wavelengths converted to the rest frame of the GRB host is shown in Figure S2. The wavelength scale in the UVOT grisms is not calibrated on board and its accuracy relies on the knowledge of the position of the source. A Mg II 2800 Å resonance line seems present with a significance larger than 4 σ, although not exactly at the right frequency location. The width of this line is larger (by a factor of two) than expected from the estimated satellite motion from the deconvolution kernel, which would be of order of 15 Å only if not already removed by the image deconvolution.

1.2 MAXI Observations

The Gas Slit Camera (GSC; (*42*)) of Monitor of All-sky X–ray Image (MAXI; (*15*)) detected GRB 130427A with one of its cameras (camera #4) at the two consecutive scan transits centered at t = 3257 s and t = 8821 s. The effective area of the GSC camera during the transit had a triangular shape with the FWZM duration of 52 seconds and the peak effective area of 3.9 cm^2 at these observations. In the present analysis, we assumed the flux within a transit to be constant. This assumption is justified considering that the time interval since the trigger ($\sim$ thousands of seconds) is much longer than the transit time ($\sim$ 50 s), and therefore the variation within the transit is negligible. MAXI usually scans a specific position in the sky once every International Space Station orbit ($\approx$ 92 min period). No significant flux was detected in the GSC Cameras from the source at the last scan transit of the GRB location before the trigger ($t = -2308$ s) and at the third scan after the trigger ($t = +14385$ s). The calibration of the energy response and details of its flight performance is described in (*43*).

1.3 BAT and XRT Spectral Analysis

We extracted several 15–150 keV BAT spectra at different time intervals starting from t = −0.1 s up to the end of the BAT observation. We fitted all these spectra with a simple power-law model and the best-fit parameters are reported in Table S4. A significant spectral evolution is apparent in the spectral results: the variation of the power-law photon index is shown in the bottom panel of Figure S3.

In the time interval between t = 195 s and t = 990 s, corresponding to the overlap between the BAT data and the XRT-WT data, we carried out a simultaneous broad band (0.3–150 keV) spectral analysis, building the BAT and XRT spectra in nine common time intervals (see Table S4). After the end of the BAT observation, the spectral analysis is based only on the 0.3–10 keV XRT data. Both the WT spectra collected between t = 990 s and t = 2021 s and the PC spectra collected after $t = 2.2 \times 10^4$ s can be well described by an absorbed power law with a column density fixed to the line-of-sight value of $1.8 \times 10^{20} \mathrm{cm}^{-2}$ plus an intrinsic (redshifted) and time varying (in the first 1 ks) absorption (see Table S4).

We are aware that fitting a slightly curved spectra with a power law introduces small biases in the column density estimate (e.g. (*44*)). Therefore, we do not consider the column density increase derived from power-law fitting of the afterglow data to be physically significant.

We have verified that no significant spectral variations occur during the XRT-PC monitoring, with the power-law index consistent with a constant value. Thus we have obtained an average PC spectrum from observation sequences 001 to 039: the results of the averaged spectral analysis are reported in Table S4.

1.4 Flux-calibrated X–ray Light Curve

We used the data from *Swift*-BAT, *Swift*-XRT and MAXI/GSC to build a flux-calibrated X–ray light curve in the 0.3–10 keV band. We used the results of the BAT spectral analysis in the

15–150 keV band to compute the conversion factor needed to obtain the $0.3-10$ keV flux from the count rate of the 64 ms BAT mask-weighted light curve up to t $= 202$ s. This conversion factor was computed with higher precision in the time interval in which the BAT and XRT data overlap using the results of the simultaneous BAT and XRT spectral analysis. The 0.3–10 keV flux for the MAXI/GSC data was obtained assuming the power-law model with a photon index $\Gamma_M = 1.8 \pm 0.1$ derived from the spectral analysis carried out on XRT data at close epochs.

The $0.3-10$ keV flux-calibrated light curve that we obtained is shown in Figure S3. The good agreement between the BAT and the XRT light curves when they overlap can be interpreted as the sign that the early X–ray light curve (t $< 10^3$ s) is probably still related to the prompt emission. For $t > 260$ s the X–ray light curve can be fitted with a double-broken power law. The first decay is steep with $\alpha_{0,x} = 3.32 \pm 0.17$ and a break at $t_{1,x} = 424 \pm 8$ s. The decay then flattens to $\alpha_{1,x} = 1.28 \pm 0.01$. A further break is needed, even if not well constrained. The second break occurs at $t_{2,x} = 48 \pm 22$ ks and the slope steepens to $\alpha_{2,x} = 1.35 \pm 0.02$. We remark that it is only thanks to the very good quality of our data that we were able to reveal this further break, whose significance is $3.8\ \sigma$, estimated through an F-test. The reported errors are derived computing the interval for a $\Delta\chi^2 = 2.71$ and are therefore the errors at 90% confidence level for one parameter of interest. A 5% error has been summed in quadrature to all the points to obtain a good fit with a reduced $\chi^2_{\rm red} = 0.9$ with 243 degrees of freedom. These decay indices and break times lie well within the distribution of those parameters as seen for the GRB population as a whole ($45,46$) [1].

We plot in Figure S4 all the X–ray light curves of the GRBs observed by *Swift*-XRT (627 GRBs as of June 4, 2013). As it can be seen, GRB 130427A has the brightest X–ray afterglow, in term of observed flux, that have ever been observed by XRT. But this is due both to the intrinsic brightness of this burst and to its proximity that enhance its fluxes. A more informative

---

[1] see http://www.swift.ac.uk/xrt_live_cat for update versions of those populations

plot is the comparison of the luminosity of this GRB with those of other bright GRBs. To this end we plot in Figure S5 the rest-frame isotropic luminosity curves for a sub-sample of GRBs observed by *Swift* (both X–ray and γ-ray luminosity). We do not show the faintest GRBs, to avoid overcrowding, and include also the brightest Fermi GRBs. As can be seen, even if GRB 130427A has the brightest X–ray afterglow in term of observed flux, it has a normal behavior in term of rest-frame luminosity. In fact, although it lies at the bright end, it is fully consistent with the range displayed by the long GRBs population at large.

1.5   Ground–based Optical/NIR Observations

The 2–m Faulkes Telescope North (FTN) robotically followed up GRB 130427A starting at t = 5.1 minutes, corresponding to $\sim$ 220 s in the rest frame. Observations were carried out with a scheduled sequence of images with the B, V, r', and i' filters (*47*) for the subsequent 5 hours. From 2.4 hrs after the detection, observations were performed also with the MITSuME Telescopes (0.5-m Akeno Observatory, 0.5-m Okayama Observatory and 1.05-m Ishigakijima Observatory; (*48*)) using the g', R_c, and I_c filters and following the optical afterglow up to 5.2 days. Data in these filters were calibrated with respect to the SDSS g', r', and i' bands, respectively. Late time observations have been performed also with the 2-m Liverpool Telescope (LT) in the time interval between 1.5 days and $\sim$ 19 days after the burst, using the Sloan filters SDSS-r' and SDSS-i'.

Calibration of the entire optical data set was carried out with respect to a common set of selected field stars. Sloan Digital Sky Survey (SDSS) catalogued stars were used for the g', r' and i' filters, while standard stars were used for the B and V filters. A summary of our calibrated data, with a log of all the observations and magnitudes of the optical counterpart in all filters, can be found in Tables S5–S9.

26

1.6 Consistency with Spectral Energy Correlations

With the exception of very few outliers, the long GRBs obey the spectral energy correlations between the rest-frame peak energy E_{peak} of their spectrum and the overall isotropically equivalent energetics E_{iso} (*28*) or isotropic peak luminosity L_{iso} (*29*). It is interesting to verify whether GRB 130427A follows these correlations as well. Figure S6 shows how GRB 130427A is located in both the "Amati" and the "Yonetoku" planes. As can be seen, it lies exactly on the best fit of both. In the same figure, the green stars show GRBs associated with a spectroscopically confirmed supernova (*14*). Note how GRB 130427A stands out.

If the break at ~ 37 ks is indeed a jet break, we can calculate the opening angle of the jet θ_{j}. With a homogeneous circumburst medium of density $n = 1$ cm^{-3} and a kinetic energy of the fireball equal to $E_{\mathrm{k,iso}} = 4 \times 10^{54}$ erg, we derive $\theta_{\mathrm{j}} \sim 3°$. The corresponding collimation corrected energy is $E_{\gamma} = 10^{51}$ erg. This makes GRB 130427A consistent (at 2σ) also with the correlation between E_{peak} and the collimation corrected energetics E_{γ} (the so-called "Ghirlanda" correlation, see (*30*)).

2 Result of the SED modeling

In this section we will try to establish if the extraordinary richness and quality of data of GRB 130427A can be explained in the simple and standard framework of a relativistic fireball running into the circumburst medium (CBM), that decelerates the fireball and produces two shocks: the forward shock, running into the CBM, and the reverse shock, running into the ejected material of the fireball. To this aim we adopt a publicly available model, developed by (*25*), that captures with some details the main physical processes we believe are occurring. On the other hand, reality is surely more complex than a simple standard model can account for. There can be more specific versions of the standard model, e.g. the fireball could be structured (namely, having an angular profile of bulk Lorentz factors and energies), the CBM could be clumped, the microphysical parameters could be varying in time and in space. However, all these are "versions" of the standard model (a collimated fireball running into the CBM) that we aim to test in its pillars, and not in its "details". We therefore ask: does the basic model reasonably account for the observed properties of this data–rich burst, or should we drastically reconsider our current general view of GRB physics?

2.1 Main assumptions

The similarity of the X–ray and optical light curves after $\sim 10^4$ seconds suggests that they are produced by the same process. The similarity of their spectral indices indicates that they belong to the same power-law spectrum. Therefore, we assume that the optical and the X–ray emission, after $\sim 10^4$ seconds, are both afterglow emission produced by a forward shock. Before 10^4 s, an extra component contributes to the emission, most notably in the X–rays. This extra component could be late prompt emission or reverse shock emission, but we will not model it.

The *Fermi*–LAT emission, above 100 MeV, is not correlated with the $\sim$ MeV emission as shown by the GBM or BAT, but shows a peak at ~ 20 seconds followed by a power-law decay

(see (*2*)). These properties suggest that the *Fermi*-LAT flux is afterglow emission produced by a forward shock. The peak of the emission indicates the onset of the afterglow. We also assume that the LAT luminosity above 100 MeV is a proxy of the bolometric luminosity of the afterglow. This should be truly independent of the radiation process originating this high-energy emission.

We assume that the radio emission could either be the low frequency part of the X–ray and optical forward shock emission, or instead be due to a reverse shock as suggested by (*31*). In the latter case our afterglow model, with no reverse shock emission, should underestimate the observed radio emission.

We assume that the achromatic break in the light curves at ~ 37 ks is a jet break.

2.2 General derived properties

Density profile — In the case of a homogeneous density, $L_{\rm bol}$ increases during the coasting phase (Γ=constant) as the observed surface area, hence as t^2. If the circumburst medium has a wind density profile $n \propto R^{-2}$, the increase of the observed surface area in the coasting phase is exactly compensated by the decreasing density, and the bolometric luminosity is constant (see, e.g., (*49*) and Eq. 11 in (*50*)). After the deceleration time, for an adiabatic fireball we have $L_{\rm bol} \propto t^{-1}$ both for the homogeneous and the wind density profile, as long as the emission occurs in the fast cooling regime. This is independent from the radiation process producing the LAT flux [e.g. synchrotron or synchrotron self–Compton (SSC)].

There exists the possibility that the GeV peak is produced by a reverse shock, possibly connected with the early optical flux (*10*). However, in this case, the decay slope of the optical flux depends on the density profile, and if it is wind–like, it is steeper than observed (*51*).

The flux decay after the peak is suggestive of an homogeneous medium if the GeV emission is SSC, since a wind density profile would make the GeV light curve substantially steeper than

observed (this point is made very explicitly by (*26*)). If the GeV is synchrotron, instead, we face the problem of explaining the nature of the very energetic photons (up to 130 GeV, rest frame) that are not expected in a shock acceleration scenario (see discussion in (*2*)). Another problem, shown in Fig. 11 of (*52*), is the over–prediction of the flux at early times ($t < 300$ s) in the *Swift*-BAT and *Fermi*-LAT energy ranges.

A wind medium has been assumed to reproduce the X–ray/optical/radio data of GRB 130427A (*31,52*) and to explain the early optical flux (*10*). In (*31*), the wind like density is preferred by comparing the predicted and observed X–ray decay slope. The slope predicted by the homogeneous density is *closer* to the observed decay. Nevertheless, they chose the wind density profile (compare the following values derived by (*31*): predicted decay in the wind case: $\alpha_x = 1.64$, in the homogeneous case: $\alpha_x = 1.14$, observed value: $\alpha_x = 1.35$). Furthermore, their wind afterglow model requires a kinetic energy $E_{\rm k,iso} \sim 10^{52}$ erg, which is only 1% of the prompt emission energy ($E_{\gamma,\rm iso} = 10^{54}$ erg), which seems rather low. This small value of $E_{\rm k,iso}$ implies rather large values of the microphysical parameters: $\epsilon_{\rm B}$ and $\epsilon_{\rm e}$ are of order unity. As a consequence, the $\epsilon_{\rm e}/\epsilon_{\rm B}$ ratio is also of order unity, and this limits the possibility to explain the GeV emission as due to the SSC process. It is then difficult to explain the detection of photons up to 130 GeV (rest frame). The normalization of the wind density profile is roughly 1,000 times smaller than expected by a typical star wind, even if this parameter is still largely uncertain for the (unknown) final phases of the life of a massive star.

Finally, we have considered a generic stratified medium, with a density $n \propto r^{-s}$, with $s = 1$ and $s = 1.5$, following (*53*), with the hope to ameliorate the problems of the pure wind–like scenario. We did find that these solutions present a deceleration peak flux, that can explain the peaked GeV emission, but are worst representations of the data at the other frequencies.

To conclude, i) the presence of the peak of the light curve and ii) the relatively flat decay slope of the light curves at all frequencies are observational evidences supporting the homoge-

neous CBM. Further support of this hypothesis is given by the small kinetic energy (requiring very large efficiencies) and the small wind normalization required by the proposed wind models. The latter are certainly possible, but the required (not mainstream) assumptions and the remaining open issues, in our opinion, are more than in the homogeneous case, that therefore we choose.

Bulk Lorentz factor — The time of the onset of the afterglow, for an assumed radiative efficiency η (defined through $E_{\text{iso}} = \eta E_{\text{k,iso}}$, where $E_{\text{k,iso}}$ is the isotropic equivalent kinetic energy of the fireball) and ISM density n, allows us to infer the value of the bulk Lorentz factor Γ_0 of the fireball before deceleration, i.e. during the coasting phase (see the discussion in (*24*) about the existing formulae). For $E_{\gamma,\text{iso}} = 10^{54}$ erg s^{-1}, $\eta = 0.1$, $t_{\text{pk}} = 20$ s and a density $n = 1$ cm^{-3} we obtain $\Gamma_0 = 505$ (using the formula in (*24*)), scaling as $\Gamma_0 \propto [E_{\gamma,\text{iso}}/(n\eta t_{\text{pk}}^3)]^{1/8}$.

Microphysical parameters: ϵ_{B} — The fraction of the available energy at the relativistic shock going to relativistic electrons and to magnetic energy is parameterized by ϵ_{e} and ϵ_{B}, respectively. The fact that the X–ray and the optical light curves share the same temporal profile in the 10^4–10^6 s interval implies that they belong to the same spectral power law branch. Therefore the characteristic frequencies, such as the injection frequency ν_{inj} or the cooling frequencies ν_{cool}, that are time–dependent, must be located outside the optical–X–ray frequency range in this time interval because, otherwise, the light curves could not be parallel. The requirement $\nu_{\text{cool}} \gtrsim 10$ keV can be fulfilled if ϵ_{B} is small (of the order of 10^{-5}–10^{-4}) implying a modest cooling (in turn implying a large ν_{cool}). This small value of ϵ_{B} is not unprecedented, since it agrees with those found by (*54*) for the GRBs detected in the GeV band by the LAT on board *Fermi*. However, more often ϵ_{B} is around $\sim 10^{-2} - 10^{-3}$ (*19,53*).

Microphysical parameters: ϵ_{e} — If the LAT emission is afterglow by a forward shock, and if it is a good proxy for the bolometric luminosity ($L_{\text{LAT}} = f L_{\text{bol}}$), we can derive ϵ_{e}. In the

fast cooling regime, L_{LAT} after the deceleration time is given by (see e.g. (*24*))

$$L_{\mathrm{LAT}} \;=\; f\,L_{\mathrm{bol}} \;=\; \frac{3f\epsilon_{\mathrm{e}}}{2}\frac{E_{\mathrm{kin,iso}}}{t}; \quad t \geq t_{\mathrm{pk}}; \qquad E_{\mathrm{kin,iso}} \;=\; E_{\gamma,\mathrm{iso}}\left(\frac{1-\eta}{\eta}\right) \tag{1}$$

therefore

$$\epsilon_{\mathrm{e}} \;\sim\; \frac{2}{3f}\frac{\eta}{1-\eta}\frac{L_{\mathrm{LAT}}}{E_{\gamma,\mathrm{iso}}}t_{\mathrm{pk}} \tag{2}$$

With $E_{\gamma,\mathrm{iso}} \sim 10^{54}$ erg, $\eta = 0.1$, $f \sim 1/6$ and $L_{\mathrm{LAT}} \sim 1.6 \times 10^{51}$ erg s^{-1} at $t_{\mathrm{pk}} \sim 15$ s (in the rest frame), we derive $\epsilon_{\mathrm{e}} \sim 10^{-2}$. Notice that *this is independent of the emission process* (see the discussion after Eq. 1 in (*55*)).

Jet opening angle and viewing angle — Defining the viewing angle θ_{v} as the angle between the line of sight and the jet axis, we have that a non–zero θ_{v} produces two breaks in the light curve, the first when $1/\Gamma = \theta_{\mathrm{j}} - \theta_{\mathrm{v}}$, and the second when $1/\Gamma = \theta_{\mathrm{j}} + \theta_{\mathrm{v}}$. With respect to an observer located on the jet axis ($\theta_{\mathrm{v}} = 0$) the off–axis viewer should see the jet break as a smoother transition (e.g. (*25,56*)). This could help make the post–break light curve decay less steeply than predicted, as in our case, up to the second break. The latter could be hidden in the optical by the host galaxy+supernova contribution to the light curve flux, but should be visible in the X–ray light curve. Note that a shallow break can also be the result of time-varying microphysical parameters: if ϵ_{B} and ϵ_{e} increase, then the light curve decays less steeply than predicted by the simplest theory, at least up to the time when ϵ_{B} and ϵ_{e} stop increasing (since the range of their values is limited). After that time, the light curve should decay as expected by the simple theory.

Radio spectra — The available radio data (as in (*31*)) indicate a rather flat spectrum, inconsistent with self–absorption and roughly consistent with $F_{\nu} \propto \nu^{1/3}$, the single electron synchrotron spectrum. This indicates that in the radio range $\nu_{\mathrm{a}} < \nu < \nu_{\mathrm{inj}}$. A small ν_{a} in turn requires a small density (of the relativistic electrons responsible for the synchrotron emission

and absorption), much smaller than the typical value of $n \sim 1$ cm^{-3}. A large $\nu_{\rm inj} \propto \gamma_{\rm inj}^2 B\Gamma$ requires large energies of the electrons.

2.3   Modeling

The model — To model the SEDs and the light curves at any frequency of GRB 130427A we use the model developed by (*25*). This model considers the synchrotron emission produced by the forward shock of an adiabatic fireball expanding into a homogeneous medium. The fireball is canonical (namely, matter, not magnetically dominated, and uniform, i.e. with radial velocity directions that are not a function of the angle from the jet axis) with an opening angle $\theta_{\rm j}$, viewed at an angle $\theta_{\rm v}$ from the axis. It accounts for the so called "jet–break", i.e the break in the light curve occurring when $1/\Gamma \sim \theta_{\rm j}$. Arrival times from the emitting volume are properly calculated. The model does not include the emission from the reverse shock, nor the contribution from synchrotron self–Compton (SSC) process. The lack of SSC is a rather serious limitation in the first (fast cooling) phases of the afterglow if the Comptonization parameter y (regulating the importance of the SSC radiation) is large, while in slow cooling the importance of SSC radiation rapidly decreases. Although we require a small $\epsilon_{\rm B}$, and $y \sim (\epsilon_{\rm e}/\epsilon_{\rm B})^{1/2}$ (see above), our modeling pertains to the slow cooling phase, therefore the lack of SSC does not affect our results. Table S10 lists the parameters of the models shown in Figure S7 (light curves) and Figure 3 of the main journal article (SEDs).

The LAT light curve — As mentioned above, the time profile of the bolometric light curve in fast cooling is independent of the emission process. If the LAT flux is indeed close to the bolometric flux, then its behavior cannot be used to discriminate between – say – synchrotron and SSC emission, provided that both processes are capable of generating high-energy photons. For GRB 130427A photons exceeding 40 GeV have been observed, with one exceeding 90 GeV, and this represents a problem for the synchrotron interpretation of the high-energy flux (see, e.g.

(*57*)). On the other hand, both SSC and inverse Compton scattering between the accelerated electrons and the prompt emission photons still present in the fireball can contribute to the GeV flux. This is even more likely if ϵ_B is indeed very small. In this case the Comptonization y parameter is bound to be large in fast cooling, making the Compton process the dominant one (unless the synchrotron typical frequencies, in the comoving frame, are so large as to make the Compton process to be in the Klein–Nishina regime).

Ghisellini et al. (*55*) discussed the case of a radiative fireball to explain the time decay of several GRBs whose γ–ray flux decayed as $t^{-1.5}$ even though their spectral slope was close to $\Gamma_\gamma = 2$. The decay slope of GRB 130427A is instead close to unity, i.e. what is expected from the bolometric luminosity decay of an adiabatic fireball. This can be explained if we consider that in GRB 130427A the afterglow onset time is close to 15 seconds: this may appear to be a very short time, but it is nevertheless later than the onset time of the bursts considered in (*55*). This relatively late onset implies that the total energy emitted in the LAT energy band is significantly lower than the prompt emission energy. If the prompt emission did not contain a sizable fraction of the kinetic energy of the fireball, then $E_k \sim E_{\gamma,\mathrm{iso}}/\eta$ and does not vary during the γ–ray emission. In other words, the fireball remains adiabatic or quasi–adiabatic. We stress that if the ISM had a wind density profile, then the initial light curve of the bolometric luminosity would be flat, without any peak. Therefore an homogeneous medium is consistent with interpreting the peak of the LAT light curve as the afterglow onset, while a wind density profile would require another interpretation for the same peak.

The XRT light curve — The model reproduces the X–ray light curve after $\sim 10^4$ seconds. We suggest that before this time the X–ray flux is dominated by late prompt emission and high–latitude radiation. By "late prompt" emission we mean radiation produced by the same mechanism(s) producing the main GRB event, but occurring later. By "high–latitude" radiation we mean the radiation from parts of the emitting surface not on axis with the line of sight. If

the surface switches off abruptly, the distant observer will see that a flux decaying in time at a predictable rate, as a result of the different arrival time of the photons combined with the different degree of beaming. Indeed, the XRT and BAT light curves are very similar as long as BAT detects the burst ($\sim$1900 seconds).

The optical–UV light curve — In Figure S7 we show how the model reproduces the best sampled optical light curves, in the R, r' and $R_{\rm c}$ filters. In the other optical bands the behavior is the same. In the model of the optical emission shown in Figure S7, we have added a constant contribution corresponding to $R = 21.3$ (flux density $\sim$0.0113 mJy) due to the host galaxy (dashed line in Figure S7).

Jet break — We interpret the break at ~ 37 ks as a jet break, corresponding to a jet open-ing angle of $\sim 3.4°$. We assume $\theta_{\rm v} = 0°$. In fact, although the assumption of a non–zero $\theta_{\rm v}$ could help to explain the shallow decay of the post–break light curve ($\propto t^{-1.3}$, shallower than predicted by the standard model, e.g. (*58*)), the late X–ray data (not affected by the host galaxy+supernova emission) do not show any further steepening of the light curve up to t ~ 45 days. We are then led to assume that the radiation emitted in the post–break phase is larger than what simple theory predicts (shown by the dotted models in Figure S7). This can be the result of having energy injection, increasing the total fireball energy which in turn increases the amount of emitted radiation. Alternatively, we can maintain a constant fireball energy, but increase the amount of energy given to the electrons (i.e. $\epsilon_{\rm e}$). We prefer the latter solution be-cause it has a lower energy requirement. We then assume that $\epsilon_{\rm e} \propto (t/t_\epsilon)^{0.6}$ after $t_\epsilon = 0.8$ day. Then, to obtain a reasonable agreement between the optical and X–ray data (circles and crosses in Figure S7) and the model, we also assume that $\epsilon_{\rm B} \propto (t/t_\epsilon)^{0.5}$ after the same $t_\epsilon = 0.8$ day. Possible evolution of the microphysical parameters at the shocks have been invoked to explain the multiwavelength light curves (in the X–ray and optical bands) of some GRBs (e.g. (*59*)).

The radio light curve — The model that we have described above, which assumes an evolution of the ϵ_e and ϵ_B parameters, over–predicts the radio flux (dot–dashed line vs squares in Figure S7). This is due to the fact that the ν_{inj} frequency is too small and it is even smaller than the self–absorption frequency ν_a. The injection frequency is $\nu_{inj} \propto \gamma_{inj}^2 B\Gamma \propto \epsilon_e^2 \epsilon_B^{1/2} t^{-3/2}$. Changing the microphysical parameters inevitably leads to other inconsistencies. An extra degree of freedom is the fraction of the electrons that are accelerated at the shock front and that produce the radiation received by the observer. Instead of assuming that the shock accelerates one electron per proton, we can assume that only a fraction $k < 1$ of the present electrons are accelerated. In this way we can increase the energy per electron and, therefore, increase ν_{inj}. This, however, must occur in such a way as to satisfy the requirement that ν_{inj} is smaller than the observed optical frequencies, at least between 10^4 and 10^6 seconds, if the optical flux remains a power law of the same slope in this time interval.

Admittedly, the complex behavior of the afterglow of GRB 130427A in the radio, optical, X–ray and γ–ray bands cannot be fully captured by a simple and standard afterglow model, e.g. synchrotron and self Compton emission by a forward shock, with non-varying microphysical parameters. Therefore we must ask ourselves: does GRB 130427A require a complete revision of our ideas about the origin of the afterglow emission? Our answer is no: the unique richness of the GRB 130427A data can still be explained within the framework of the standard model. It surely requires extra assumptions, but not a radical change.
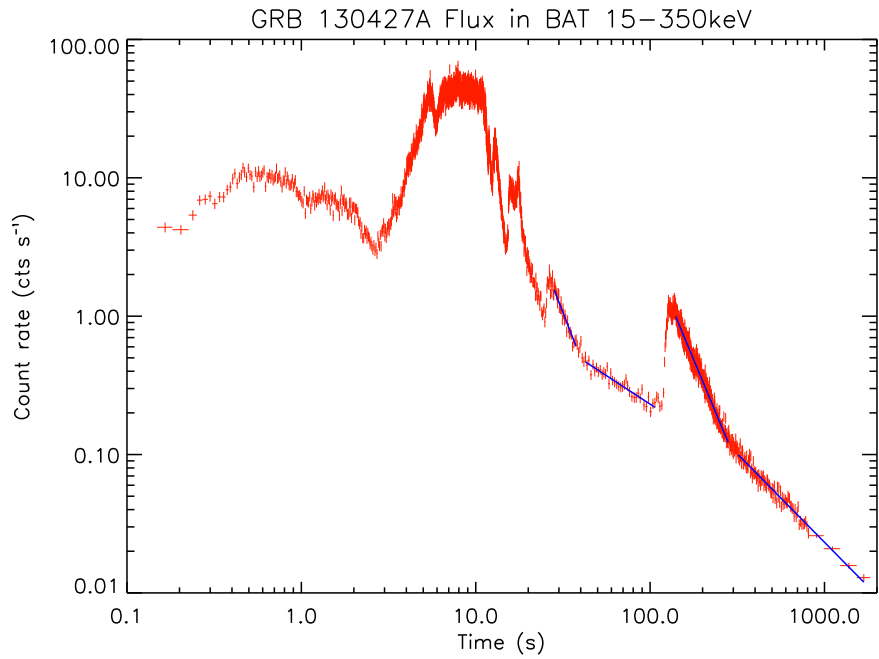
Figure S1. BAT mask-weighted light curve showing the count rate in the 15–350 keV energy range. The rate has been corrected for the significant deadtime over the main peak of the event, with a maximum correction factor of 1.72. The 4 blue curves shown are power-law fits with indices $\alpha_1 = 3.25 \pm 0.04$, $\alpha_2 = 0.82 \pm 0.04$, $\alpha_3 = 3.02 \pm 0.03$, and $\alpha_4 = 1.28 \pm 0.04$, from earlier to later times.
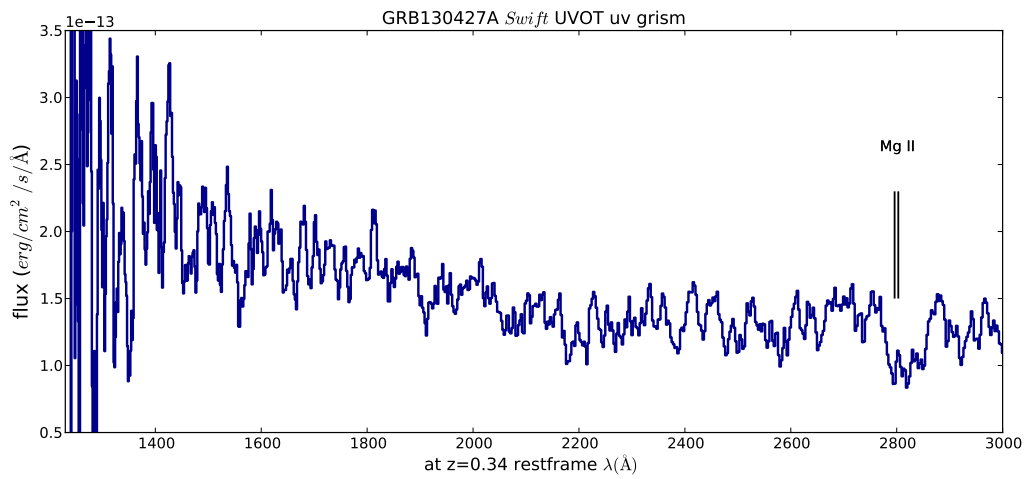
Figure S2. The *Swift* UVOT spectrum with wavelengths converted to the rest frame of the GRB host. The strongest absorption feature in the spectrum corresponds to the redshifted Mg II 2800 Å resonance line. The flux above 2200 Å (in the rest frame) is overestimated due to second order contamination.
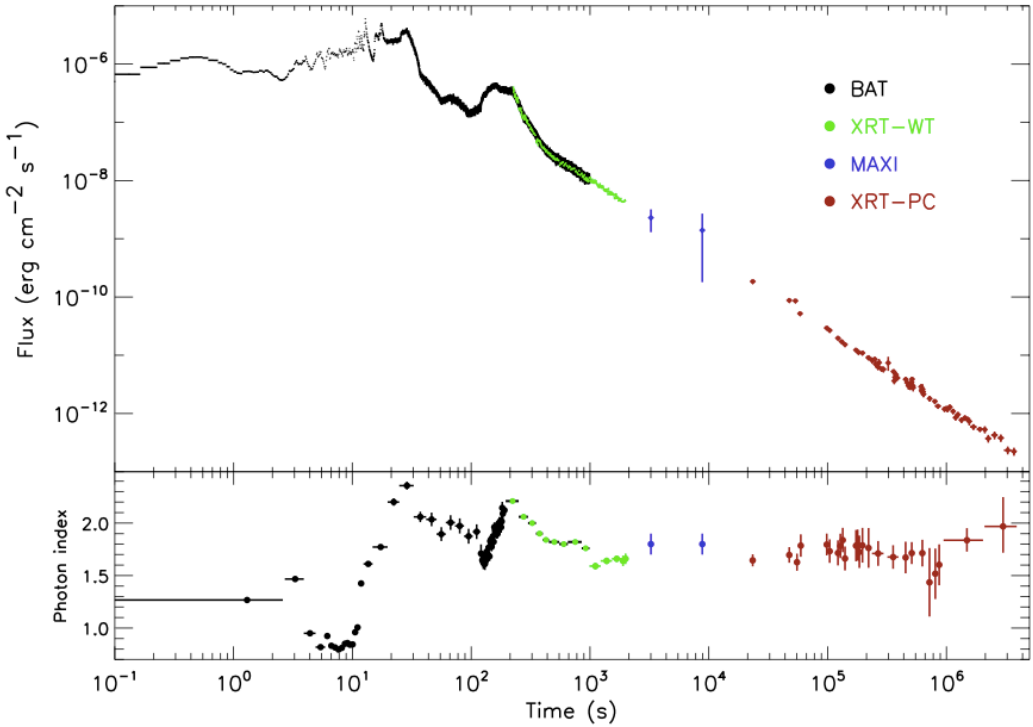
Figure S3. Top panel: composite BAT/XRT light curve starting since 0.3 s after the GBM trigger. The XRT light curve in the $0.3-10$ keV energy range is shown together with the BAT light curve extrapolated to the same energy range assuming a power-law model in the 15–150 keV energy range. The conversion from count rates to fluxes has been performed using the spectral parameters listed in Table S4. Blue points correspond to the flux by MAXI obtained assuming $\Gamma = 1.8\pm0.1$ (see bottom panel) to compute the conversion factor from the count rate. Bottom panel: the values of the photon index obtained adopting a simple power-law model in the spectral analysis.
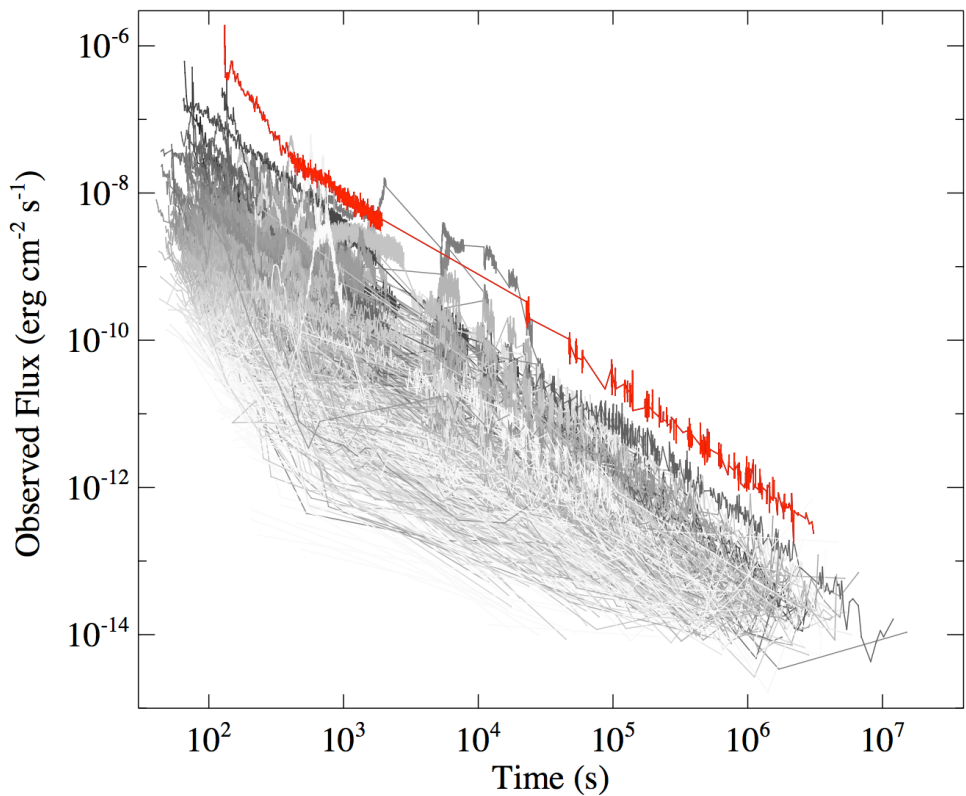
Figure S4. Comparison of all the 627 GRBs observed by XRT (as of June 4, 2013). In terms of the observed flux, the X–ray afterglow of GRB 130427A, in red color in this figure, is the brightest so far observed.
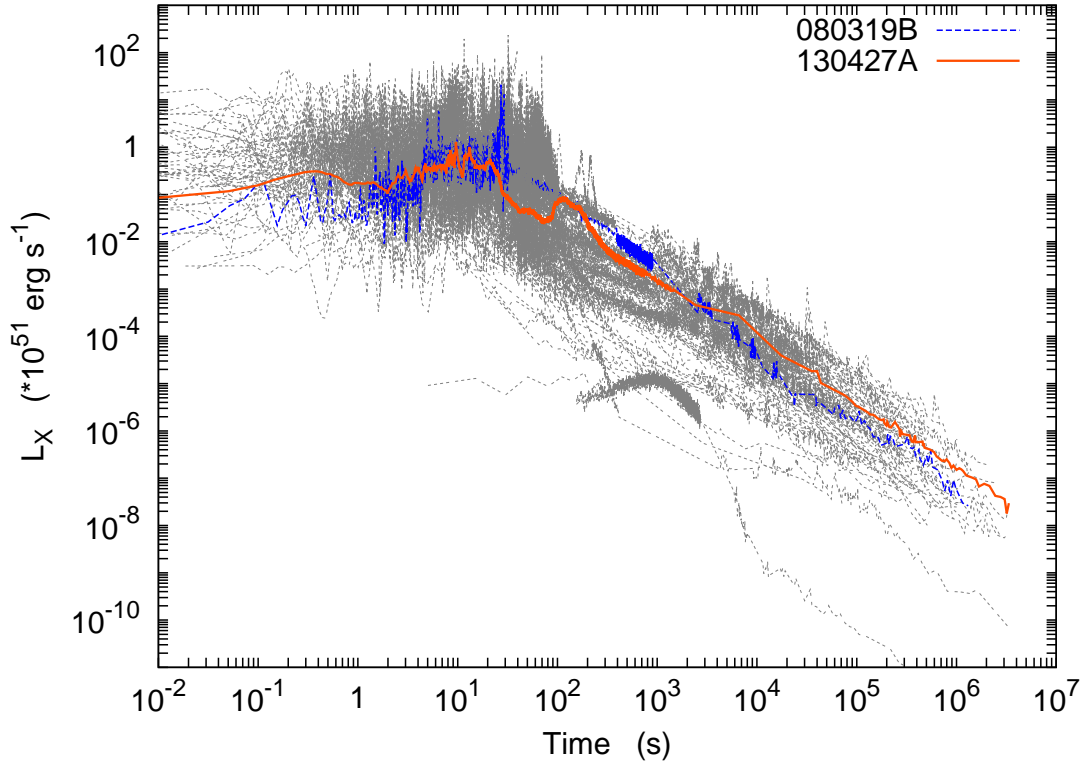
Figure S5. Rest–frame isotropic X–ray luminosity light curves for a selected sample of long, relatively bright GRBs (grey curves). For comparison we show in orange and blue the rest–frame luminosity for GRB 130427A and GRB 080319B (*naked-eye*), respectively. For each event we also plot the BAT γ-ray luminosity. The behavior and luminosity of GRB 130427A is within the range of long GRBs population at large.
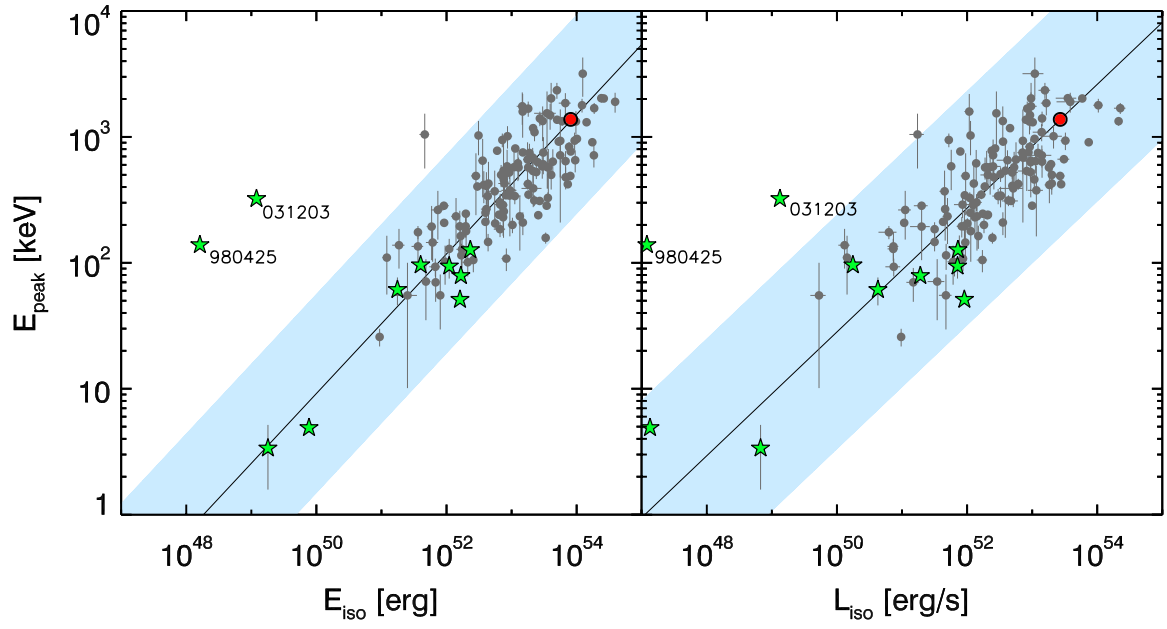
Figure S6. The Amati (left panel) and Yonetoku (right panel) correlations. Grey filled circles refer to the sample studied in (*60*). Their power–law fit is shown as a solid dark line. Green stars correspond to GRBs associated with a spectroscopically confirmed supernova. The shaded region represents the 3σ scatter of the distribution of points around this best fit line. GRB 130427A (red circle) lies exactly on the best fit of both correlations.

Line	E_k	ϵ_e	ϵ_B	n	p	θ_j	t_k	α_k	t_e	α_e	t_B	α_B
	erg/s			cm^{-3}		deg	days		days		days	
dotted	5e54	0.027	1.e–5	1	2.3	3.4°	...	...	...	...	...	...
solid	5e54	0.027	1.e–5	1	2.3	3.4°	0.2	–0.8	0.8	0.6	0.8	0.5

Table S10. List of parameters used for the model plotted in the Figure S7. We assumed $k = (t/t_k)^{\alpha_k}$ after t_k (and same functions for ϵ_e and ϵ_B).
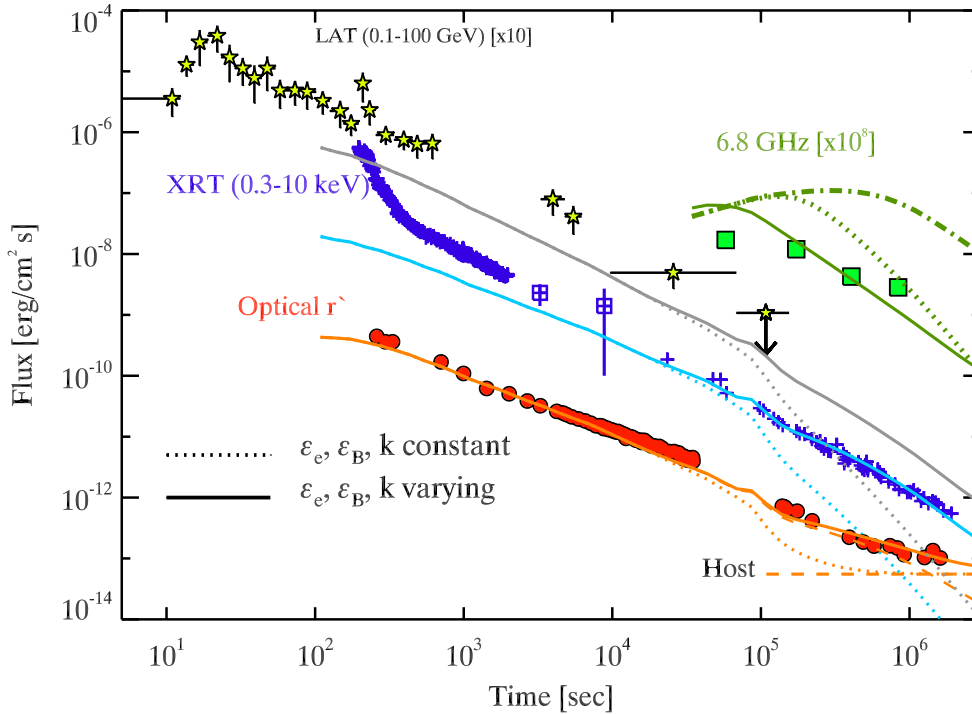
Figure S7. The optical, X–ray, γ–ray and radio light curves are interpreted as forward shock afterglow synchrotron emission, as derived applying the van Eerten et al. model. Dotted lines corresponds to the first line in Table S10, namely ϵ_e, ϵ_B and the fraction k of accelerated electrons are constant. The solid line corresponds to the model when varying these microphysical parameters. The dot–dashed line shown only for the radio band, corresponds to the model with only ϵ_e and ϵ_B varying in time and with constant k.

Date	ObsID	Mode	t_{start}	t_{stop}	Exposure
2013-04-27	00554620000	WT	195.0	2021.0	1826.0
2013-04-27	00554620001	PC	22895.7	23992.1	1091.3
2013-04-27	00554620002	PC	46969.2	48157.6	1183.7
2013-04-27	00554620003	PC	53000.0	57444.6	1166.2
2013-04-28	00554620010	PC	58984.1	59841.1	616.8
2013-04-28	00554620011	PC	86273.6	86308.9	34.9
2013-04-28	00554620012	PC	97700.2	98876.9	1171.2
2013-04-28	00554620013	PC	103473.2	104649.1	1171.2
2013-04-28	00554620014	PC	121583.6	122777.0	1188.7
2013-04-28	00554620015	PC	127497.0	128688.0	1186.2
2013-04-28	00554620016	PC	133486.8	134678.1	1186.2
2013-04-28	00554620017	PC	139453.2	140626.6	1168.7
2013-04-29	00554620018	PC	172691.4	173887.4	1191.2
2013-04-29	00554620019	PC	178457.6	179653.6	1191.2
2013-04-29	00554620020	PC	184342.2	185538.2	1191.2
2013-04-29	00554620021	PC	195806.2	197002.1	1191.2
2013-04-29	00554620022	PC	214255.0	214282.9	27.4
2013-04-29	00554620023	PC	220516.4	226200.7	1163.7
2013-04-30	00554620024	PC	236492.8	284417.9	2235.0
2013-04-30	00554620025	PC	231962.4	295404.9	1263.6
2013-05-01	00554620026	PC	318431.4	387978.9	2949.3
2013-05-01	00554620027	PC	323916.2	393026.9	2861.8
2013-05-02	00554620028	PC	443986.8	480197.1	2474.8
2013-05-02	00554620029	PC	450022.2	462502.1	1033.8
2013-05-03	00554620030	PC	495862.2	520641.9	4879.1
2013-05-03	00554620031	PC	501622.2	525617.9	4033.1
2013-05-04	00554620032	PC	611311.6	636145.9	4869.6
2013-05-04	00554620033	PC	617072.2	642158.1	3628.5
2013-05-05	00554620034	PC	711244.4	734065.1	948.9
2013-05-05	00554620035	PC	717012.8	728662.1	946.4

Table S1. List of XRT Observations.

Date	ObsID	Mode	t_{start}	t_{stop}	Exposure
2013-05-06	00554620036	PC	790108.6	815075.0	2577.2
2013-05-06	00554620037	PC	795861.2	820847.0	1872.9
2013-05-07	00554620038	PC	842938.6	890245.4	3316.4
2013-05-07	00554620039	PC	848698.4	896015.6	3875.7
2013-05-08	00554620040	PC	946138.4	1005185.9	3338.8
2013-05-08	00554620041	PC	963096.0	999986.7	4597.4
2013-05-09	00554620042	PC	1015070.2	1044940.6	5096.9
2013-05-09	00554620043	PC	1009222.2	1034321.2	4382.7
2013-05-10	00554620044	PC	1101436.4	1137558.1	3211.5
2013-05-10	00554620045	PC	1130278.0	1170759.0	3109.1
2013-05-11	00554620046	PC	1199567.8	1223006.9	3668.5
2013-05-11	00554620047	PC	1205387.8	1230084.8	4922.1
2013-05-12	00554620048	PC	1268802.2	1291864.2	3238.9
2013-05-12	00554620049	PC	1274530.4	1297614.9	3081.6
2013-05-13	00554620050	PC	1356452.8	1398086.9	2839.4
2013-05-13	00554620051	PC	1362212.8	1403733.9	2205.1
2013-05-14	00554620052	PC	1441798.4	1472380.9	5084.4
2013-05-14	00554620053	PC	1447558.0	1477901.1	4430.1
2013-05-15	00554620054	PC	1535337.9	1580847.9	3793.3
2013-05-15	00554620055	PC	1529578.2	1575387.9	2739.5
2013-05-16	00554620056	PC	1614928.2	1689963.7	2966.7
2013-05-16	00554620057	PC	1620680.4	1695761.2	2931.8
2013-05-17	00554620058	PC	1707466.4	1759866.0	571.8
2013-05-17	00554620059	PC	1701445.8	1713010.1	77.4
2013-05-18	00554620060	PC	1789327.4	1847062.2	3149.0
2013-05-18	00554620061	PC	1793698.4	1852829.5	3151.5
2013-05-19	00554620062	PC	1880294.8	1950499.0	3316.3
2013-05-19	00554620063	PC	1874537.6	1957165.6	4520.0
2013-05-20	00554620064	PC	2007777.3	2030161.2	2302.4
2013-05-20	00554620065	PC	2002047.2	2025770.0	2372.4

Table S1. Continued.

45

Date	ObsID	Mode	t_{start}	t_{stop}	Exposure
2013-05-21	00554620066	PC	2093589.6	2128184.9	4123.0
2013-05-21	00554620067	PC	2099349.3	2122434.4	1470.9
2013-05-22	00554620068	PC	2180242.6	2215409.1	1815.5
2013-05-22	00554620069	PC	2185857.8	2210360.0	4065.6
2013-05-24	00554620070	PC	2358988.2	2382118.1	1643.2
2013-05-24	00554620071	PC	2364683.4	2389163.0	4567.5
2013-05-26	00554620072	PC	2520513.0	2543605.9	112.4
2013-05-26	00554620073	PC	2514753.2	2537833.9	127.4
2013-05-28	00554620074	PC	2687649.2	2712052.5	2584.7
2013-05-28	00554620075	PC	2693409.2	2723792.9	3341.4
2013-05-30	00554620076	PC	2838150.4	2873300.8	2517.3
2013-05-30	00554620077	PC	2843910.2	2878100.5	182.3
2013-05-31	00554620078	PC	2958738.2	2970872.2	1530.9
2013-06-01	00554620079	PC	3034154.0	3058480.6	4260.4
2013-06-01	00554620080	PC	3039807.5	3064297.5	3498.7
2013-06-03	00554620081	PC	3207534.7	3219986.9	964.0
2013-06-03	00554620082	PC	3196010.0	3224848.9	112.4
2013-06-05	00554620083	PC	3385650.6	3426578.8	2632.1
2013-06-05	00554620084	PC	3380735.1	3420857.9	3184.0
2013-06-07	00554620085	PC	3524157.8	3548402.3	3611.1
2013-06-07	00554620086	PC	3518412.8	3542624.9	3443.8
2013-06-09	00554620087	PC	3691594.0	3726982.5	1970.4
2013-06-09	00554620088	PC	3697361.2	3698268.8	904.0
2013-06-11	00554620089	PC	3870322.0	3906218.0	2627.1
2013-06-11	00554620090	PC	3864659.2	3899309.9	1223.7

Table S1. Continued.

Mode	t_{start}	t_{stop}	r	R
WT	195	250	30	60
WT	250	300	20	60
WT	300	350	15	60
WT	350	400	12	60
WT	400	450	10	60
WT	450	550	9	60
WT	550	650	8	60
WT	650	850	7	60
WT	850	1150	4	60
WT	1150	1851	3	60
PC	22874	54172	4	32
PC	57429	59534	2	27

Table S2. The value, expressed in pixels (1 pixel = 2.36″), of the inner r and outer R radius of the annular extraction region adopted to take into account the pile-up corrections, when needed.

t_{start}	Time interval	Flux	Magnitude	Filter
s	s	mJy	mag	
432.9	19.4	55.86 ± 1.78	12.10 ± 0.04	v
606.5	19.7	38.62 ± 1.18	12.50 ± 0.03	v
779.2	19.7	31.23 ± 0.98	12.73 ± 0.04	v
1104.7	19.7	19.01 ± 0.67	13.27 ± 0.04	v
1278.7	19.7	16.55 ± 0.60	13.42 ± 0.04	v
1450.9	19.7	13.92 ± 0.54	13.61 ± 0.04	v
1623.2	19.2	11.90 ± 0.50	13.78 ± 0.05	v
1795.5	176.8	10.87 ± 0.42	13.88 ± 0.04	v
1972.3	15.8	10.77 ± 0.51	13.89 ± 0.05	v
221178.8	79.8	0.042 ± 0.025	19.91 ± 0.54	v
271227.3	24196.7	0.019 ± 0.016	20.72 ± 0.69	v
358892.1	23111.9	0.050 ± 0.009	19.70 ± 0.19	v
462312.3	46771.8	0.020 ± 0.006	20.68 ± 0.32	v
520269.5	394.6	0.017 ± 0.010	20.84 ± 0.53	v
612573.7	23590.4	0.021 ± 0.006	20.66 ± 0.30	v
797123.6	64580.4	0.016 ± 0.006	20.94 ± 0.37	v
884582.0	79902.1	0.006 ± 0.009	22.03 ± 1.07	v
981779.5	63164.5	0.012 ± 0.004	21.23 ± 0.37	v
1102735.3	110088.8	0.015 ± 0.005	21.00 ± 0.35	v
1270046.2	128057.8	0.015 ± 0.005	20.97 ± 0.35	v
1443096.2	29287.8	0.018 ± 0.006	20.81 ± 0.33	v
1615695.2	208.9	0.035 ± 0.015	20.11 ± 0.42	v
1800561.6	149962.6	0.014 ± 0.005	21.08 ± 0.39	v
2008769.3	206654.8	0.013 ± 0.004	21.15 ± 0.34	v

Table S3. UVOT Observation log, reporting the interval of time over which observations have been collected since t_{start}. Observations where reliable photometry could not be extracted are not included in the table. Magnitudes have not been corrected for Galactic absorption along the line of sight (E_{B-V} = 0.020 mag; (*61*)). The estimate extinctions in the different filters are: A_v = 0.062 mag, A_b = 0.079 mag, A_u = 0.096 mag, A_{w1} = 0.132 mag, A_{m2} = 0.193 mag, and A_{w2} = 0.175 mag. Corrected magnitudes have been converted into flux densities, F_ν, following (*62*).

t_{start}	Time interval	Flux	Magnitude	Filter
s	s	mJy	mag	
531.3	19.8	111.71 ± 41.54	11.48 ± 0.56	b
705.2	19.7	30.25 ± 1.04	12.90 ± 0.04	b
877.1	19.7	23.12 ± 0.71	13.19 ± 0.04	b
1202.9	19.7	16.05 ± 0.48	13.59 ± 0.03	b
1376.9	19.7	13.11 ± 0.39	13.81 ± 0.03	b
1549.3	19.7	11.28 ± 0.34	13.97 ± 0.04	b
1721.3	19.6	10.22 ± 0.32	14.08 ± 0.04	b
1894.7	19.7	9.96 ± 0.31	14.10 ± 0.04	b
214507.9	6340.9	0.076 ± 0.013	19.40 ± 0.18	b
271079.9	24046.0	0.048 ± 0.009	19.88 ± 0.21	b
358368.0	23153.4	0.026 ± 0.004	20.55 ± 0.16	b
461774.3	46475.9	0.020 ± 0.003	20.81 ± 0.16	b
519400.6	428.8	0.026 ± 0.005	20.55 ± 0.21	b
611734.9	23645.7	0.016 ± 0.003	21.05 ± 0.19	b
728222.7	68475.9	0.017 ± 0.003	21.03 ± 0.22	b
849077.3	35320.8	0.012 ± 0.003	21.40 ± 0.28	b
963459.9	80954.7	0.011 ± 0.002	21.47 ± 0.20	b
1101871.9	110119.4	0.012 ± 0.002	21.37 ± 0.21	b
1269219.5	128289.1	0.008 ± 0.002	21.79 ± 0.29	b
1442233.5	93695.0	0.013 ± 0.002	21.33 ± 0.21	b
1615186.9	144686.9	0.009 ± 0.005	21.62 ± 0.49	b
1799842.9	150091.8	0.009 ± 0.003	21.70 ± 0.30	b
2008110.9	206950.9	0.012 ± 0.003	21.37 ± 0.24	b

Table S3. Continued.

t_{start}	Time interval	Flux	Magnitude	Filter
s	s	mJy	mag	
506.3	19.8	52.75 ± 18.58	11.19 ± 0.35	u
680.3	5.9	25.06 ± 1.61	12.00 ± 0.07	u
852.4	19.7	21.97 ± 0.73	12.14 ± 0.04	u
1178.1	19.7	14.55 ± 0.44	12.59 ± 0.04	u
1352.2	19.7	11.68 ± 0.34	12.83 ± 0.03	u
1524.0	19.7	10.67 ± 0.31	12.93 ± 0.03	u
1696.3	19.7	9.42 ± 0.29	13.06 ± 0.04	u
1870.0	19.7	8.52 ± 0.26	13.17 ± 0.04	u
54067.8	93.6	0.335 ± 0.017	16.69 ± 0.06	u
59780.3	83.7	0.281 ± 0.018	16.88 ± 0.07	u
140625.7	25.7	0.113 ± 0.021	17.86 ± 0.20	u
214423.1	11801.4	0.049 ± 0.005	18.76 ± 0.13	u
294833.7	143.7	0.044 ± 0.007	18.89 ± 0.17	u
358106.2	23165.6	0.028 ± 0.002	19.38 ± 0.10	u
461504.8	41819.3	0.016 ± 0.002	20.01 ± 0.14	u
514722.8	10921.3	0.025 ± 0.005	19.48 ± 0.20	u
611315.7	30848.3	0.013 ± 0.001	20.22 ± 0.12	u
717016.8	11200.7	0.016 ± 0.002	20.01 ± 0.17	u
795865.5	83118.5	0.011 ± 0.001	20.40 ± 0.13	u
884045.8	79408.9	0.007 ± 0.001	20.81 ± 0.23	u
980566.2	63564.7	0.008 ± 0.001	20.69 ± 0.15	u
1101440.8	110128.2	0.009 ± 0.001	20.59 ± 0.18	u
1218440.7	69083.4	0.003 ± 0.001	21.91 ± 0.45	u
1356456.8	121447.2	0.005 ± 0.001	21.25 ± 0.22	u
1530645.2	142918.7	0.006 ± 0.001	21.02 ± 0.25	u
1759348.6	173006.9	0.005 ± 0.001	21.18 ± 0.24	u
1945016.0	178788.1	0.003 ± 0.001	21.67 ± 0.33	u
2187205.5	27676.8	0.002 ± 0.002	22.38 ± 0.93	u

Table S3. Continued.

t_{start}	Time interval	Flux	Magnitude	Filter
s	s	mJy	mag	
556.8	20.0	52.22 ± 13.70	11.52 ± 0.27	*white*
729.7	20.0	28.38 ± 11.16	12.18 ± 0.39	*white*
924.4	150.0	18.79 ± 4.55	12.63 ± 0.26	*white*
271152.9	24121.4	0.041 ± 0.003	19.28 ± 0.09	*white*
358629.3	23141.3	0.028 ± 0.002	19.67 ± 0.06	*white*
462042.5	46641.4	0.019 ± 0.001	20.10 ± 0.07	*white*
519834.3	428.8	0.018 ± 0.002	20.13 ± 0.12	*white*
612153.5	23645.9	0.014 ± 0.001	20.43 ± 0.09	*white*
728641.2	68476.1	0.013 ± 0.002	20.52 ± 0.16	*white*
849450.8	35125.5	0.011 ± 0.002	20.68 ± 0.13	*white*
963818.3	80879.6	0.008 ± 0.001	21.04 ± 0.09	*white*
1102303.2	110109.7	0.008 ± 0.001	21.03 ± 0.11	*white*
1269632.1	128173.5	0.009 ± 0.001	20.88 ± 0.10	*white*
1442664.2	93347.3	0.008 ± 0.001	21.00 ± 0.12	*white*
1615440.4	248.8	0.004 ± 0.002	21.88 ± 0.43	*white*
1800201.6	150031.8	0.007 ± 0.001	21.19 ± 0.12	*white*
2008439.3	206801.2	0.006 ± 0.001	21.28 ± 0.11	*white*

Table S3. Continued.

t_{start}	Time interval	Flux	Magnitude	Filter
s	s	mJy	mag	
353.1	50.0	34.74 ± 6.30	11.16 ± 0.20	$w1$
482.0	19.7	32.06 ± 1.03	11.25 ± 0.04	$w1$
656.0	19.7	21.16 ± 0.60	11.70 ± 0.03	$w1$
828.1	19.7	16.80 ± 0.47	11.95 ± 0.03	$w1$
1153.9	19.7	10.77 ± 0.32	12.43 ± 0.04	$w1$
1327.9	19.7	9.71 ± 0.29	12.54 ± 0.04	$w1$
1499.8	19.7	8.34 ± 0.26	12.71 ± 0.04	$w1$
1672.1	19.7	7.11 ± 0.23	12.88 ± 0.04	$w1$
1845.7	19.7	6.76 ± 0.22	12.94 ± 0.04	$w1$
22815.1	1194.5	0.653 ± 0.007	15.47 ± 0.01	$w1$
47984.9	182.5	0.297 ± 0.012	16.33 ± 0.05	$w1$
53830.4	232.7	0.223 ± 0.009	16.64 ± 0.05	$w1$
59602.1	173.7	0.219 ± 0.011	16.66 ± 0.06	$w1$
128683.9	11937.3	0.075 ± 0.004	17.83 ± 0.07	$w1$
214259.1	11885.6	0.030 ± 0.002	18.81 ± 0.11	$w1$
236774.5	13349.6	0.041 ± 0.004	18.48 ± 0.13	$w1$
265634.6	18809.6	0.024 ± 0.002	19.08 ± 0.13	$w1$
363955.3	24048.8	0.014 ± 0.002	19.67 ± 0.13	$w1$
444708.8	35515.3	0.008 ± 0.002	20.32 ± 0.23	$w1$
502837.9	22755.6	0.012 ± 0.002	19.81 ± 0.14	$w1$
618246.5	23802.0	0.009 ± 0.002	20.10 ± 0.19	$w1$
802790.8	76130.4	0.010 ± 0.002	19.95 ± 0.15	$w1$
890059.6	57528.8	0.006 ± 0.002	20.57 ± 0.29	$w1$
993711.0	40534.5	0.007 ± 0.001	20.39 ± 0.19	$w1$
1131487.8	98462.9	0.005 ± 0.001	20.90 ± 0.20	$w1$
1275703.7	127929.6	0.004 ± 0.002	21.13 ± 0.29	$w1$
1448766.3	126581.8	0.004 ± 0.001	20.95 ± 0.21	$w1$
1621349.3	52161.3	0.005 ± 0.001	20.76 ± 0.30	$w1$
1794872.4	162196.8	0.002 ± 0.001	21.78 ± 0.38	$w1$
2014458.7	195819.5	0.004 ± 0.001	21.09 ± 0.23	$w1$

Table S3. Continued.

t_{start}	Time interval	Flux	Magnitude	Filter
s	s	mJy	mag	
353.1	50.0	34.13 ± 4.96	11.04 ± 0.17	$m2$
457.4	19.7	30.34 ± 0.87	11.17 ± 0.04	$m2$
630.8	19.7	21.01 ± 0.59	11.57 ± 0.03	$m2$
803.4	19.7	16.65 ± 0.48	11.82 ± 0.04	$m2$
1129.2	19.7	10.41 ± 0.34	12.33 ± 0.04	$m2$
1303.1	19.7	9.337 ± 0.31	12.45 ± 0.04	$m2$
1475.2	19.7	8.067 ± 0.28	12.61 ± 0.04	$m2$
1647.4	19.7	7.130 ± 0.26	12.74 ± 0.05	$m2$
1821.1	176.3	6.797 ± 0.22	12.79 ± 0.04	$m2$
1997.4	15.2	6.246 ± 0.27	12.88 ± 0.05	$m2$
47550.8	428.7	0.264 ± 0.009	16.32 ± 0.04	$m2$
53475.6	349.8	0.193 ± 0.008	16.66 ± 0.05	$m2$
59336.5	260.7	0.196 ± 0.011	16.64 ± 0.07	$m2$
87292.1	180.3	0.110 ± 0.009	17.26 ± 0.10	$m2$
98763.5	5907.9	0.104 ± 0.007	17.33 ± 0.09	$m2$
122321.9	12191.3	0.059 ± 0.003	17.95 ± 0.06	$m2$
139989.5	375.8	0.053 ± 0.005	18.07 ± 0.12	$m2$
173759.1	11782.3	0.045 ± 0.004	18.24 ± 0.11	$m2$
196860.3	144.0	0.032 ± 0.006	18.62 ± 0.22	$m2$
221262.8	15506.9	0.033 ± 0.004	18.58 ± 0.15	$m2$
249788.6	15840.9	0.028 ± 0.004	18.73 ± 0.15	$m2$
283890.8	273.8	0.026 ± 0.004	18.82 ± 0.18	$m2$
363616.4	24067.6	0.017 ± 0.002	19.28 ± 0.12	$m2$
444349.9	35669.7	0.013 ± 0.002	19.61 ± 0.15	$m2$
502317.7	23096.3	0.009 ± 0.001	19.95 ± 0.16	$m2$
617743.7	23967.1	0.008 ± 0.001	20.13 ± 0.18	$m2$
734000.3	68784.9	0.007 ± 0.002	20.26 ± 0.26	$m2$
843514.9	46539.8	0.006 ± 0.001	20.42 ± 0.21	$m2$
946786.2	87218.6	0.007 ± 0.001	20.26 ± 0.14	$m2$
1130971.3	98643.9	0.005 ± 0.001	20.61 ± 0.16	$m2$
1275202.4	128217.1	0.003 ± 0.001	21.15 ± 0.27	$m2$
1448249.9	126914.6	0.003 ± 0.001	21.12 ± 0.23	$m2$
1621063.5	52243.3	0.003 ± 0.001	21.00 ± 0.33	$m2$
1794370.2	162459.1	0.002 ± 0.001	21.35 ± 0.27	$m2$
2014064.7	195913.4	0.003 ± 0.001	21.13 ± 0.20	$m2$

Table S3. Continued.

t_{start}	Time interval	Flux	Magnitude	Filter
s	s	mJy	mag	
353.1	50.0	29.93 ± 5.21	11.16 ± 0.20	$w2$
408.6	19.7	29.27 ± 0.91	11.18 ± 0.04	$w2$
582.1	19.7	19.99 ± 0.55	11.60 ± 0.03	$w2$
754.9	19.7	13.85 ± 0.37	12.00 ± 0.03	$w2$
1080.3	19.7	10.43 ± 0.29	12.30 ± 0.04	$w2$
1254.4	19.7	7.98 ± 0.23	12.60 ± 0.04	$w2$
1426.5	19.7	7.33 ± 0.22	12.69 ± 0.04	$w2$
1598.9	19.6	6.15 ± 0.19	12.88 ± 0.04	$w2$
1771.0	177.5	5.85 ± 0.17	12.93 ± 0.04	$w2$
1948.6	15.4	5.51 ± 0.20	13.00 ± 0.05	$w2$
46973.3	571.7	0.235 ± 0.006	16.42 ± 0.03	$w2$
53004.4	4461.0	0.183 ± 0.005	16.69 ± 0.04	$w2$
58983.6	347.7	0.161 ± 0.007	16.83 ± 0.05	$w2$
86277.7	1000.0	0.103 ± 0.003	17.32 ± 0.04	$w2$
97704.2	6824.8	0.079 ± 0.002	17.61 ± 0.03	$w2$
121587.5	12484.0	0.056 ± 0.002	17.98 ± 0.04	$w2$
139481.7	501.7	0.052 ± 0.003	18.07 ± 0.07	$w2$
172695.6	12662.9	0.035 ± 0.002	18.48 ± 0.04	$w2$
195811.2	18792.7	0.028 ± 0.002	18.71 ± 0.09	$w2$
220854.4	15776.7	0.026 ± 0.003	18.80 ± 0.12	$w2$
249610.0	15820.9	0.020 ± 0.002	19.09 ± 0.15	$w2$
283612.0	273.8	0.019 ± 0.003	19.13 ± 0.17	$w2$
363277.5	24068.6	0.013 ± 0.002	19.55 ± 0.12	$w2$
443990.9	35769.8	0.009 ± 0.001	19.97 ± 0.13	$w2$
501625.9	23519.8	0.008 ± 0.001	20.09 ± 0.12	$w2$
617076.2	24133.1	0.007 ± 0.001	20.13 ± 0.12	$w2$
711248.4	22746.2	0.005 ± 0.001	20.59 ± 0.21	$w2$
790112.9	65517.9	0.006 ± 0.001	20.29 ± 0.11	$w2$
878285.9	68494.2	0.003 ± 0.001	21.06 ± 0.23	$w2$
992498.7	41147.9	0.004 ± 0.001	20.80 ± 0.17	$w2$
1205391.8	69804.4	0.004 ± 0.001	20.83 ± 0.15	$w2$
1391283.4	138764.5	0.003 ± 0.001	21.07 ± 0.16	$w2$
1541102.2	131900.6	0.003 ± 0.001	21.07 ± 0.20	$w2$
1793702.7	162768.5	0.003 ± 0.001	21.05 ± 0.16	$w2$
2013540.1	195989.7	0.003 ± 0.001	21.09 ± 0.18	$w2$

Table S3. Continued.

Instrument	t_{start}	t_{stop}	N_H	Γ	Normalization	χ^2 (d.o.f.)
	s	s	10^{22} cm^{-2}		ph cm^{-2} s^{-1} keV^{-1} @ 50 keV	
BAT	0.0	2.8	-	1.27 ± 0.03	0.45 ± 0.01	0.98 (57)
BAT	2.8	4.0	-	1.47 ± 0.04	0.39 ± 0.01	1.74 (57)
BAT	4.0	5.0	-	0.95 ± 0.03	1.15 ± 0.02	1.10 (57)
BAT	5.0	6.0	-	0.82 ± 0.02	2.36 ± 0.04	1.91 (57)
BAT	6.0	6.5	-	0.92 ± 0.03	2.22 ± 0.04	1.48 (57)
BAT	6.5	7.0	-	0.83 ± 0.03	2.87 ± 0.05	1.49 (57)
BAT	7.0	7.5	-	0.82 ± 0.03	2.91 ± 0.05	1.31 (57)
BAT	7.5	8.0	-	0.79 ± 0.03	3.17 ± 0.05	1.48 (57)
BAT	8.0	8.5	-	0.81 ± 0.03	3.12 ± 0.05	1.55 (57)
BAT	8.5	9.0	-	0.85 ± 0.03	3.15 ± 0.05	1.58 (57)
BAT	9.0	9.4	-	0.86 ± 0.03	2.98 ± 0.05	1.47 (57)
BAT	9.4	9.9	-	0.84 ± 0.03	3.03 ± 0.05	1.28 (57)
BAT	9.9	10.4	-	0.84 ± 0.03	2.92 ± 0.05	1.58 (57)
BAT	10.4	10.9	-	0.96 ± 0.03	2.82 ± 0.05	1.43 (57)
BAT	10.9	11.4	-	1.01 ± 0.03	2.58 ± 0.05	1.87 (57)
BAT	11.4	12.5	-	1.42 ± 0.03	1.28 ± 0.02	2.04 (57)
BAT	12.5	14.9	-	1.61 ± 0.03	0.68 ± 0.01	1.39 (57)
BAT	14.9	19.9	-	1.77 ± 0.03	0.41 ± 0.01	0.96 (57)
BAT	19.9	24.9	-	2.20 ± 0.06	0.094 ± 0.003	0.56 (57)
BAT	24.9	32.9	-	2.36 ± 0.06	0.073 ± 0.002	0.94 (57)
BAT	32.9	41.9	-	2.06 ± 0.08	0.038 ± 0.002	1.18 (57)
BAT	41.9	51.2	-	2.04 ± 0.11	0.025 ± 0.002	0.97 (57)
BAT	51.2	61.2	-	1.90 ± 0.11	0.023 ± 0.001	0.60 (57)
BAT	61.2	73.2	-	2.00 ± 0.12	0.019 ± 0.001	1.13 (57)
BAT	73.2	87.2	-	1.97 ± 0.12	0.016 ± 0.001	1.02 (57)
BAT	87.2	103.2	-	1.88 ± 0.11	0.015 ± 0.001	0.96 (57)
BAT	103.2	119.4	-	1.92 ± 0.11	0.015 ± 0.001	1.28 (57)
BAT	119.4	122.7	-	1.71 ± 0.14	0.030 ± 0.003	1.35 (57)
BAT	122.7	125.7	-	1.65 ± 0.10	0.053 ± 0.003	1.09 (57)
BAT	125.7	127.7	-	1.62 ± 0.10	0.069 ± 0.004	1.05 (57)

Table S4. Parameters of the spectral analysis of *Swift* data. The values of a simple power-law fit are reported for different time intervals. BAT and XRT spectra were simultaneously fitted for 195 s $<$ t $<$ 990 s.

Instrument	t_{start}	t_{stop}	N_H	Γ	Normalization	χ^2 (d.o.f.)
	s	s	10^{22} cm^{-2}		ph cm^{-2} s^{-1} keV^{-1} @ 50 keV	
BAT	127.7	129.7	-	1.67 ± 0.10	0.072 ± 0.004	0.72 (57)
BAT	129.7	131.7	-	1.61 ± 0.09	0.074 ± 0.004	1.04 (57)
BAT	131.7	133.7	-	1.64 ± 0.10	0.065 ± 0.004	0.72 (57)
BAT	133.7	135.7	-	1.73 ± 0.09	0.066 ± 0.003	1.25 (57)
BAT	135.7	137.7	-	1.69 ± 0.08	0.072 ± 0.003	0.88 (57)
BAT	137.7	139.7	-	1.69 ± 0.08	0.072 ± 0.003	1.14 (57)
BAT	139.7	141.7	-	1.77 ± 0.07	0.067 ± 0.003	0.68 (57)
BAT	141.7	143.7	-	1.68 ± 0.08	0.061 ± 0.003	1.04 (57)
BAT	143.7	145.7	-	1.83 ± 0.08	0.052 ± 0.002	0.74 (57)
BAT	145.7	147.7	-	1.84 ± 0.07	0.051 ± 0.002	1.10 (57)
BAT	147.7	149.7	-	1.77 ± 0.07	0.052 ± 0.002	0.74 (57)
BAT	149.7	151.7	-	1.83 ± 0.07	0.050 ± 0.002	0.99 (57)
BAT	151.7	153.7	-	1.87 ± 0.07	0.045 ± 0.002	0.88 (57)
BAT	153.7	155.7	-	1.82 ± 0.07	0.044 ± 0.002	0.90 (57)
BAT	155.7	157.7	-	1.96 ± 0.07	0.038 ± 0.002	0.88 (57)
BAT	157.7	159.7	-	1.93 ± 0.07	0.038 ± 0.001	0.73 (57)
BAT	159.7	161.7	-	1.94 ± 0.07	0.038 ± 0.001	1.14 (57)
BAT	161.7	163.7	-	1.93 ± 0.07	0.034 ± 0.001	0.93 (57)
BAT	163.7	165.7	-	1.90 ± 0.07	0.035 ± 0.001	0.63 (57)
BAT	165.7	167.7	-	1.90 ± 0.07	0.033 ± 0.001	0.86 (57)
BAT	167.7	169.7	-	1.99 ± 0.08	0.030 ± 0.001	0.58 (57)
BAT	169.7	171.7	-	1.95 ± 0.08	0.029 ± 0.001	1.14 (57)
BAT	171.7	173.7	-	2.01 ± 0.08	0.026 ± 0.001	0.88 (57)
BAT	173.7	175.7	-	1.96 ± 0.08	0.026 ± 0.001	0.63 (57)
BAT	175.7	177.7	-	2.01 ± 0.08	0.025 ± 0.001	1.02 (57)
BAT	177.7	179.7	-	1.96 ± 0.09	0.024 ± 0.001	0.81 (57)
BAT	179.7	181.7	-	2.02 ± 0.09	0.024 ± 0.001	0.73 (57)
BAT	181.7	183.7	-	2.14 ± 0.09	0.022 ± 0.001	0.66 (57)
BAT	183.7	185.7	-	2.09 ± 0.09	0.024 ± 0.001	0.84 (57)
BAT	185.7	195.7	-	2.12 ± 0.05	0.022 ± 0.001	0.75 (57)

Table S4. Continued.

Instrument	t_{start}	t_{stop}	N_H	Γ	Normalization	χ^2 (d.o.f.)
	s	s	10^{22} cm^{-2}		ph cm^{-2} s^{-1} keV^{-1} @ 1 keV	
BAT + XRT-WT	195	250	0.30 ± 0.02	2.21 ± 0.01	79 ± 2	1.59 (331)
BAT + XRT-WT	250	300	0.13 ± 0.02	2.06 ± 0.02	23 ± 1	1.12 (299)
BAT + XRT-WT	300	350	0.06 ± 0.02	2.00 ± 0.02	13.7 ± 0.7	1.26 (286)
BAT + XRT-WT	350	400	0.04 ± 0.06	1.90 ± 0.02	7.9 ± 0.4	1.20 (247)
BAT + XRT-WT	400	450	0.04 ± 0.02	1.84 ± 0.02	5.3 ± 0.3	1.08 (251)
BAT + XRT-WT	450	550	0.08 ± 0.02	1.82 ± 0.02	3.9 ± 0.2	1.35 (330)
BAT + XRT-WT	550	650	0.14 ± 0.02	1.80 ± 0.02	3.1 ± 0.1	1.21 (308)
BAT + XRT-WT	650	850	0.14 ± 0.01	1.82 ± 0.01	2.4 ± 0.1	1.22 (391)
BAT + XRT-WT	850	990	0.14 ± 0.01	1.76 ± 0.02	1.66 ± 0.04	1.06 (377)
XRT-WT	990	1230	0.09 ± 0.01	1.59 ± 0.03	1.22 ± 0.03	0.94 (378)
XRT-WT	1230	1530	0.10 ± 0.01	1.64 ± 0.03	0.93 ± 0.02	1.12 (401)
XRT-WT	1530	1830	0.10 ± 0.01	1.66 ± 0.03	0.72 ± 0.02	1.04 (359)
XRT-WT	1830	1963	0.10 ± 0.01	1.64 ± 0.05	0.59 ± 0.03	1.13 (206)
XRT-WT	1963	2021	0.10 ± 0.01	1.66 ± 0.05	0.67 ± 0.03	1.06 (219)
XRT-PC	22896	896016	0.06 ± 0.01	1.72 ± 0.04	$(1.61 \pm 0.05) \times 10^{-3}$	0.91 (322)

Table S4. Continued.

t_{start}	Exposure	Flux	Magnitude	Filter
s	s	mJy	mag	
591.1	10.0	49.12 ± 0.23	12.21 ± 0.01	i'
838.9	30.0	37.26 ± 0.17	12.51 ± 0.01	i'
1165.9	60.0	22.87 ± 0.10	13.04 ± 0.01	i'
2317.9	180.0	10.55 ± 0.05	13.88 ± 0.01	i'
2914.3	120.0	8.53 ± 0.04	14.11 ± 0.01	i'
3595.3	180.0	6.97 ± 0.03	14.33 ± 0.01	i'
4539.1	10.20	4.69 ± 0.04	14.76 ± 0.01	i'
4780.3	30.0	5.09 ± 0.05	14.67 ± 0.01	i'
5088.1	60.0	4.65 ± 0.04	14.77 ± 0.01	i'
5556.1	120.0	4.61 ± 0.04	14.78 ± 0.01	i'
6219.1	180.0	4.12 ± 0.04	14.90 ± 0.01	i'
6807.1	120.0	3.90 ± 0.03	14.96 ± 0.01	i'
7443.1	180.0	3.53 ± 0.03	15.07 ± 0.01	i'
8037.1	10.0	3.69 ± 0.14	15.02 ± 0.04	i'
8271.1	30.0	3.36 ± 0.06	15.12 ± 0.02	i'
8577.1	60.0	3.30 ± 0.06	15.14 ± 0.02	i'
9033.1	120.0	3.07 ± 0.03	15.22 ± 0.01	i'
9693.1	180.0	2.99 ± 0.03	15.25 ± 0.01	i'
10287.1	120.0	2.93 ± 0.03	15.27 ± 0.01	i'
10923.1	180.0	2.80 ± 0.03	15.32 ± 0.01	i'
11805.1	10.0	2.29 ± 0.11	15.54 ± 0.05	i'
12051.1	30.0	2.24 ± 0.06	15.56 ± 0.03	i'
12357.1	60.0	2.33 ± 0.04	15.52 ± 0.02	i'
12819.1	120.0	2.33 ± 0.04	15.52 ± 0.02	i'
13479.1	180.0	2.21 ± 0.04	15.58 ± 0.02	i'
14073.1	120.0	2.10 ± 0.04	15.63 ± 0.02	i'
14739.1	180.0	2.05 ± 0.04	15.66 ± 0.02	i'
15639.1	10.0	1.75 ± 0.12	15.83 ± 0.07	i'
15873.1	30.0	1.64 ± 0.06	15.90 ± 0.04	i'
16173.1	60.0	1.88 ± 0.05	15.75 ± 0.03	i'
16641.1	120.0	1.80 ± 0.03	15.80 ± 0.02	i'
17271.1	180.0	1.66 ± 0.03	15.89 ± 0.02	i'
173691.1	1500.0	0.129 ± 0.006	18.66 ± 0.05	i'
220551.1	1500.0	0.124 ± 0.002	18.70 ± 0.02	i'

Table S5. Faulkes Telescope North observation log. Magnitudes have not been corrected for Galactic absorption along the line of sight ($E_{B-V} = 0.020$ mag; (*61*)). The estimate extinctions in the different filters are: $A_{i'} = 0.040$ mag, $A_{r'} = 0.052$ mag, $A_V = 0.062$ mag, and $A_B = 0.079$ mag. Corrected magnitudes have been converted into flux densities, F_ν, following (*62*).

t_{start}	Exposure	Flux	Magnitude	Filter
s	s	mJy	mag	
310.9	10.0	91.29 ± 0.17	11.553 ± 0.002	r'
348.1	10.0	74.34 ± 0.14	11.776 ± 0.002	r'
382.9	10.0	74.27 ± 0.14	11.777 ± 0.002	r'
754.9	30.0	34.68 ± 0.06	12.604 ± 0.002	r'
1047.1	60.0	22.43 ± 0.04	13.077 ± 0.002	r'
1477.9	120.0	12.73 ± 0.02	13.692 ± 0.002	r'
2073.1	180.0	10.41 ± 0.02	13.910 ± 0.002	r'
2731.9	120.0	7.92 ± 0.02	14.207 ± 0.002	r'
3328.9	180.0	6.61 ± 0.02	14.403 ± 0.002	r'
4279.3	30.0	5.35 ± 0.03	14.634 ± 0.007	r'
4699.9	30.0	5.03 ± 0.03	14.700 ± 0.007	r'
4972.9	60.0	4.72 ± 0.02	14.768 ± 0.005	r'
5373.1	120.0	4.36 ± 0.02	14.856 ± 0.005	r'
5968.9	180.0	4.02 ± 0.01	14.944 ± 0.003	r'
6625.3	120.0	3.72 ± 0.02	15.027 ± 0.005	r'
7207.9	180.0	3.42 ± 0.01	15.119 ± 0.004	r'
7786.9	30.0	3.11 ± 0.08	15.223 ± 0.027	r'
8191.3	30.0	3.12 ± 0.04	15.220 ± 0.013	r'
8466.1	60.0	3.10 ± 0.02	15.225 ± 0.008	r'
8860.3	120.0	2.92 ± 0.02	15.289 ± 0.006	r'
9453.1	180.0	2.67 ± 0.01	15.380 ± 0.005	r'
10107.1	120.0	2.57 ± 0.02	15.430 ± 0.007	r'
10684.9	180.0	2.45 ± 0.01	15.483 ± 0.006	r'
11563.3	30.0	2.35 ± 0.03	15.525 ± 0.016	r'
11968.9	30.0	2.26 ± 0.03	15.567 ± 0.017	r'
12241.9	60.0	2.17 ± 0.02	15.615 ± 0.011	r'
12633.1	120.0	2.11 ± 0.02	15.644 ± 0.009	r'
13231.3	180.0	2.05 ± 0.02	15.675 ± 0.008	r'
13888.9	120.0	1.95 ± 0.02	15.730 ± 0.010	r'
14493.1	180.0	1.86 ± 0.01	15.783 ± 0.008	r'
15384.1	30.0	1.75 ± 0.07	15.844 ± 0.041	r'
15793.3	30.0	1.65 ± 0.04	15.910 ± 0.025	r'
16060.3	60.0	1.77 ± 0.03	15.833 ± 0.017	r'
16468.9	120.0	1.78 ± 0.02	15.824 ± 0.013	r'
17035.9	180.0	1.63 ± 0.02	15.923 ± 0.011	r'
17671.3	120.0	1.53 ± 0.02	15.995 ± 0.015	r'
175258.3	1200.0	0.123 ± 0.008	18.731 ± 0.070	r'

Table S5. Continued.

t_{start}	Exposure	Flux	Magnitude	Filter
s	s	mJy	mag	
526.3	10.0	38.22 ± 0.10	12.513 ± 0.003	V
4462.9	10.0	4.50 ± 0.06	14.836 ± 0.013	V
7966.3	10.0	2.39 ± 0.05	15.522 ± 0.021	V
11740.3	10.0	1.63 ± 0.04	15.941 ± 0.027	V
15568.9	10.0	1.35 ± 0.05	16.145 ± 0.042	V
469.3	10.0	41.29 ± 0.15	12.622 ± 0.004	B
672.1	30.0	27.40 ± 0.07	13.067 ± 0.003	B
928.3	60.0	18.92 ± 0.03	13.469 ± 0.002	B
1294.9	120.0	11.96 ± 0.02	13.967 ± 0.002	B
1840.3	180.0	8.36 ± 0.02	14.356 ± 0.002	B
2562.1	120.0	5.56 ± 0.02	14.798 ± 0.003	B
3100.9	180.0	4.89 ± 0.01	14.939 ± 0.003	B
4396.3	10.0	3.83 ± 0.16	15.203 ± 0.047	B
4618.9	30.0	3.52 ± 0.03	15.294 ± 0.010	B
4863.1	60.0	3.41 ± 0.02	15.329 ± 0.007	B
5197.3	120.0	3.36 ± 0.02	15.344 ± 0.005	B
5736.1	180.0	3.00 ± 0.01	15.468 ± 0.004	B
6447.1	120.0	2.61 ± 0.01	15.622 ± 0.006	B
6975.1	180.0	2.51 ± 0.01	15.663 ± 0.005	B
7965.1	10.0	1.98 ± 0.05	15.921 ± 0.028	B
8115.1	30.0	2.12 ± 0.03	15.843 ± 0.017	B
8355.1	60.0	2.09 ± 0.02	15.861 ± 0.011	B
8691.1	120.0	2.16 ± 0.02	15.826 ± 0.008	B
9213.1	180.0	1.88 ± 0.01	15.973 ± 0.007	B
9927.1	120.0	1.83 ± 0.02	16.005 ± 0.009	B
10455.1	180.0	1.70 ± 0.01	16.086 ± 0.008	B
11157.1	240.0	1.60 ± 0.01	16.154 ± 0.007	B
11679.1	10.0	1.67 ± 0.05	16.107 ± 0.035	B
11883.1	30.0	1.43 ± 0.03	16.276 ± 0.022	B
12129.1	60.0	1.43 ± 0.02	16.272 ± 0.016	B
12465.1	120.0	1.52 ± 0.02	16.210 ± 0.012	B
12999.1	180.0	1.49 ± 0.01	16.224 ± 0.010	B
13719.1	120.0	1.37 ± 0.02	16.318 ± 0.015	B
14253.1	180.0	1.35 ± 0.02	16.337 ± 0.012	B
14979.1	240.0	1.28 ± 0.02	16.389 ± 0.013	B
15837.1	100.2	1.26 ± 0.03	16.409 ± 0.023	B
16293.1	120.0	1.14 ± 0.03	16.520 ± 0.025	B
16809.1	180.0	1.15 ± 0.02	16.513 ± 0.022	B
17499.1	120.0	1.12 ± 0.03	16.539 ± 0.029	B

Table S5. Continued.

t_{start}	Exposure	Flux	Magnitude	Filter
s	s	mJy	mag	
146703.7	600.0	0.171 ± 0.002	18.356 ± 0.010	i'
220285.9	600.0	0.118 ± 0.002	18.759 ± 0.012	i'
393591.1	600.0	0.055 ± 0.002	19.594 ± 0.027	i'
489248.5	600.0	0.051 ± 0.001	19.664 ± 0.023	i'
578223.1	900.0	0.038 ± 0.001	19.988 ± 0.034	i'
739861.3	900.0	0.032 ± 0.001	20.175 ± 0.036	i'
829746.1	900.0	0.030 ± 0.005	20.247 ± 0.180	i'
920669.5	900.0	0.026 ± 0.010	20.400 ± 0.410	i'
1260787.3	900.0	0.028 ± 0.002	20.312 ± 0.083	i'
1435981.9	900.0	0.022 ± 0.001	20.576 ± 0.042	i'
1611121.9	900.0	0.020 ± 0.001	20.673 ± 0.054	i'
139209.1	600.0	0.148 ± 0.001	18.526 ± 0.010	r'
144618.1	600.0	0.143 ± 0.001	18.564 ± 0.012	r'
149664.1	600.0	0.131 ± 0.001	18.663 ± 0.012	r'
221105.5	600.0	0.085 ± 0.001	19.127 ± 0.011	r'
392943.7	600.0	0.046 ± 0.002	19.800 ± 0.048	r'
488596.9	600.0	0.038 ± 0.001	19.998 ± 0.020	r'
577276.3	900.0	0.032 ± 0.001	20.164 ± 0.021	r'
738914.5	900.0	0.033 ± 0.001	20.150 ± 0.026	r'
828793.3	900.0	0.030 ± 0.003	20.256 ± 0.110	r'
919716.7	900.0	0.024 ± 0.001	20.518 ± 0.029	r'
1259841.1	900.0	0.021 ± 0.001	20.631 ± 0.028	r'
1435035.7	900.0	0.028 ± 0.001	20.349 ± 0.022	r'
1610174.5	900.0	0.021 ± 0.001	20.653 ± 0.033	r'

Table S6. Liverpool telescope observation log. Magnitudes have not been corrected for Galactic absorption along the line of sight (E_{B-V} = 0.020 mag; (*61*)). The estimate extinctions in the different filters are: $A_{i'}$ = 0.040 mag, and $A_{r'}$ = 0.052 mag. Corrected magnitudes have been converted into flux densities, F_ν, following (*62*).

t_{start}	Exposure	Flux	Magnitude	Filter
s	s	mJy	mag	
8802.7	420.0	3.40 ± 0.13	15.108 ± 0.041	i'
9330.7	600.0	3.03 ± 0.06	15.233 ± 0.022	i'
9988.9	600.0	2.88 ± 0.04	15.289 ± 0.016	i'
10978.9	1200.0	2.77 ± 0.04	15.333 ± 0.015	i'
12297.1	1200.0	2.45 ± 0.04	15.464 ± 0.016	i'
13614.1	1200.0	2.14 ± 0.03	15.613 ± 0.017	i'
15331.3	1800.0	2.03 ± 0.03	15.669 ± 0.018	i'
17310.1	1800.0	1.79 ± 0.04	15.805 ± 0.027	i'
19219.9	1800.0	1.70 ± 0.03	15.858 ± 0.020	i'
21660.1	2640.0	1.41 ± 0.03	16.063 ± 0.021	i'
24162.1	1800.0	1.29 ± 0.03	16.163 ± 0.024	i'
26145.7	1800.0	1.25 ± 0.03	16.194 ± 0.026	i'
28130.5	1800.0	1.19 ± 0.03	16.250 ± 0.026	i'
30106.3	1800.0	1.14 ± 0.03	16.296 ± 0.027	i'
32091.7	1800.0	1.06 ± 0.03	16.371 ± 0.030	i'
34733.5	3000.0	0.94 ± 0.04	16.504 ± 0.044	i'
8802.7	420.0	2.79 ± 0.06	15.339 ± 0.024	r'
9330.7	600.0	2.82 ± 0.03	15.330 ± 0.012	r'
9988.9	600.0	2.65 ± 0.04	15.396 ± 0.015	r'
10978.9	1200.0	2.51 ± 0.04	15.456 ± 0.016	r'
12297.1	1200.0	2.20 ± 0.04	15.600 ± 0.021	r'
13614.1	1200.0	2.02 ± 0.03	15.692 ± 0.017	r'
15331.3	1800.0	1.81 ± 0.02	15.812 ± 0.014	r'
17310.1	1800.0	1.62 ± 0.02	15.930 ± 0.014	r'
19219.9	1800.0	1.45 ± 0.02	16.051 ± 0.015	r'
21660.1	2640.0	1.33 ± 0.02	16.144 ± 0.016	r'
24162.1	1800.0	1.17 ± 0.02	16.284 ± 0.018	r'
26145.7	1800.0	1.17 ± 0.02	16.284 ± 0.018	r'
28130.5	1800.0	1.11 ± 0.02	16.344 ± 0.021	r'
30106.3	1800.0	0.99 ± 0.02	16.467 ± 0.023	r'
32091.7	1800.0	0.93 ± 0.02	16.531 ± 0.026	r'
34733.5	3000.0	0.93 ± 0.12	16.533 ± 0.136	r'
9330.7	600.0	2.341 ± 0.022	15.555 ± 0.026	g'
9988.9	600.0	2.231 ± 0.013	15.608 ± 0.015	g'
10978.9	1200.0	2.143 ± 0.011	15.652 ± 0.014	g'
12297.1	1200.0	1.879 ± 0.010	15.794 ± 0.015	g'
13614.1	1200.0	1.655 ± 0.009	15.932 ± 0.016	g'
15331.3	1800.0	1.550 ± 0.009	16.003 ± 0.017	g'
17310.1	1800.0	1.424 ± 0.009	16.095 ± 0.018	g'
19219.9	1800.0	1.243 ± 0.009	16.242 ± 0.019	g'
21660.1	2640.0	1.088 ± 0.008	16.387 ± 0.020	g'
24162.1	1800.0	1.030 ± 0.009	16.447 ± 0.023	g'
26145.7	1800.0	0.939 ± 0.009	16.548 ± 0.026	g'
28130.5	1800.0	0.842 ± 0.009	16.667 ± 0.029	g'
30106.3	1800.0	0.824 ± 0.010	16.689 ± 0.032	g'
32091.7	1800.0	0.751 ± 0.011	16.790 ± 0.041	g'
34733.5	3000.0	0.673 ± 0.013	16.909 ± 0.054	g'

Table S7. Akeno Observatory observation log. Magnitudes have not been corrected for Galactic absorption along the line of sight (E_{B-V} = 0.020 mag; (*61*)). The estimate extinctions in the different filters are: $A_{i'}$ = 0.040 mag, $A_{r'}$ = 0.052 mag, $A_{g'}$ = 0.072 mag. Corrected magnitudes have been converted into flux densities, F_ν, following (*62*).

t_{start}	Exposure	Flux	Magnitude	Filter
s	s	mJy	mag	
12416.5	1800.0	2.32 ± 0.05	15.525 ± 0.023	i'
14475.1	1800.0	2.22 ± 0.05	15.570 ± 0.022	i'
16525.3	1800.0	1.94 ± 0.05	15.716 ± 0.028	i'
18576.1	1800.0	1.90 ± 0.08	15.741 ± 0.045	i'
20770.3	2040.0	1.70 ± 0.06	15.860 ± 0.042	i'
25421.5	2760.0	1.26 ± 0.04	16.188 ± 0.037	i'
28165.9	1800.0	1.11 ± 0.05	16.321 ± 0.049	i'
30216.7	1800.0	0.99 ± 0.06	16.447 ± 0.063	i'
32269.9	1800.0	0.92 ± 0.12	16.527 ± 0.147	i'
34950.1	2940.0	0.846 ± 0.054	16.619 ± 0.069	i'
12416.5	1800.0	1.93 ± 0.04	15.741 ± 0.025	r'
14475.1	1800.0	1.80 ± 0.04	15.815 ± 0.027	r'
16525.3	1800.0	1.67 ± 0.06	15.897 ± 0.042	r'
18576.1	1800.0	1.43 ± 0.03	16.064 ± 0.026	r'
20770.3	2040.0	1.42 ± 0.06	16.072 ± 0.044	r'
25421.5	2760.0	1.15 ± 0.04	16.300 ± 0.040	r'
28165.9	1800.0	1.04 ± 0.25	16.410 ± 0.264	r'
30216.7	1800.0	0.89 ± 0.05	16.581 ± 0.057	r'
32269.9	1800.0	0.84 ± 0.06	16.639 ± 0.072	r'
34950.1	2940.0	0.81 ± 0.05	16.682 ± 0.064	r'
12416.5	1800.0	1.841 ± 0.030	15.816 ± 0.045	g'
14475.1	1800.0	1.437 ± 0.027	16.085 ± 0.051	g'
16525.3	1800.0	1.326 ± 0.035	16.172 ± 0.073	g'
18576.1	1800.0	1.228 ± 0.023	16.254 ± 0.051	g'
20770.3	2040.0	1.208 ± 0.029	16.273 ± 0.067	g'
25421.5	2760.0	1.017 ± 0.022	16.460 ± 0.059	g'
28165.9	1800.0	0.847 ± 0.021	16.658 ± 0.069	g'
30216.7	1800.0	0.839 ± 0.032	16.668 ± 0.104	g'
32269.9	1800.0	0.784 ± 0.052	16.745 ± 0.181	g'

Table S8. Okayama Observatory observation log. Magnitudes have not been corrected for Galactic absorption along the line of sight (E_{B-V} = 0.020 mag; (*61*)). The estimate extinctions in the different filters are: $A_{i'}$ = 0.040 mag, $A_{r'}$ = 0.052 mag, and $A_{g'}$ = 0.072 mag. Corrected magnitudes have been converted into flux densities, F_ν, following (*62*).

t_{start}	Exposure	Flux	Magnitude	Filter
s	s	mJy	mag	
110172.1	1200.0	0.225 ± 0.012	18.057 ± 0.059	i'
112361.5	1200.0	0.220 ± 0.030	18.081 ± 0.150	i'
116807.5	1500.0	0.193 ± 0.017	18.225 ± 0.095	i'
200004.7	1800.0	0.099 ± 0.007	18.942 ± 0.079	i'
202120.3	1800.0	0.103 ± 0.008	18.906 ± 0.083	i'
205012.9	3180.0	0.103 ± 0.008	18.902 ± 0.080	i'
455880.1	540.0	0.048 ± 0.010	19.723 ± 0.219	i'
110172.1	1200.0	0.215 ± 0.007	18.123 ± 0.035	r'
112361.5	1200.0	0.192 ± 0.007	18.246 ± 0.039	r'
116807.5	1500.0	0.194 ± 0.008	18.233 ± 0.041	r'
200004.7	1800.0	0.103 ± 0.007	18.918 ± 0.059	r'
202120.3	1800.0	0.091 ± 0.006	19.059 ± 0.067	r'
205012.9	3180.0	0.090 ± 0.005	19.068 ± 0.063	r'
455880.1	540.0	0.039 ± 0.008	19.972 ± 0.226	r'
110172.1	1080.0	0.161 ± 0.002	18.453 ± 0.041	g'
112361.5	1200.0	0.153 ± 0.002	18.507 ± 0.040	g'
116807.5	1080.0	0.126 ± 0.006	18.726 ± 0.143	g'
200004.7	1800.0	0.078 ± 0.001	19.241 ± 0.052	g'
202120.3	1800.0	0.078 ± 0.002	19.250 ± 0.063	g'
205012.9	3000.0	0.075 ± 0.002	19.275 ± 0.064	g'
455880.1	540.0	0.030 ± 0.003	20.227 ± 0.232	g'

Table S9. Ishigakijima Observatory observation log. Magnitudes have not been corrected for Galactic absorption along the line of sight (E_{B-V} = 0.020 mag; (*61*)). The estimate extinctions in the different filters are: $A_{i'}$ = 0.040 mag, $A_{r'}$ = 0.052 mag, and $A_{g'}$ = 0.072 mag. Corrected magnitudes have been converted into flux densities, F_ν, following (*62*).